Microtubules control cellular shape and coherence in amoeboid migrating cells

Aglaja Kopf[1], Jörg Renkawitz[1,2], Robert Hauschild[1], Irute Girkontaite[3], Kerry Tedford[4], Jack Merrin[1], Oliver Thorn-Seshold[5], Dirk Trauner[6], Hans Häcker[7], Klaus-Dieter Fischer[4], Eva Kiermaier[1,8],* and Michael Sixt[1],*

[1]Institute of Science and Technology (IST) Austria, 3400 Klosterneuburg, Austria.
[2]Biomedical Center (BMC), Walter Brendel Center of Experimental Medicine, Institute of Cardiovascular Physiology and Pathophysiology, Klinikum der Universität, LMU Munich, 81377 Munich, Germany.
[3]Department of Immunology, State Research Institute Centre for Innovative Medicine, LT-08409 Vilnius, Lithuania.
[4]Institute of Biochemistry and Cell Biology, Otto-von-Guericke University, 39120 Magdeburg, Germany.
[5]Department of Pharmacy, Ludwig-Maximilians-University Munich, 81377 Munich, Germany.
[6]Department of Chemistry, New York University, New York, NY 10003, USA.
[7]Department of Infectious Diseases, St. Jude Children's Research Hospital, Memphis, TN 38105, USA.
[8]Life and Medical Science (LIMES) Institute, University of Bonn, 53113 Bonn, Germany.

*Correspondence to Michael Sixt; Sixt@ist.ac.at, phone +43 2243 90003801 or Eva Kiermaier ekiermai@uni-bonn.de, phone +49 228-73-62819

1   **Cells navigating through tissues face a fundamental challenge: while multiple cellular**
2   **protrusions explore different paths through the complex geometry of an interstitial matrix**
3   **the cell needs to avoid becoming too long or ramified, which might ultimately lead to a loss**
4   **of physical coherence. How a cell surveys its own shape to inform the actomyosin system**
5   **to retract entangled or stretched protrusions is not understood. Here, we demonstrate that**
6   **spatially distinct microtubule (MT) dynamics regulate amoeboid cell migration by locally**
7   **specifying the retraction of explorative protrusions. In migrating dendritic cells (DCs), the**
8   **microtubule organizing center (MTOC) guides the path through a three dimensional (3D)**
9   **interstitium and local MT depolymerization in protrusions remote from the MTOC triggers**
10   **myosin II dependent contractility via the RhoA exchange factor Lfc. Depletion of Lfc leads**
11   **to aberrant myosin localization, thereby causing two effects that rate-limit locomotion: i)**
12   **impaired cell edge coordination during path-finding and ii) defective adhesion-resolution.**
13   **Such compromised cell shape control is particularly hindering when cells navigate through**
14   **geometrically complex microenvironments, where it leads to entanglement and ultimately**
15   **fragmentation of the cell body. Our data demonstrate that MTs control cell shape and**
16   **coherence by locally controlling protrusion-retraction dynamics of the actomyosin system.**
17
18

19   How different cell types maintain their typical shape and how cells with a dynamic shape

20   prevent loss of physical coherence is poorly understood. This issue becomes particularly

21   critical in migrating cells, in which protrusion of the leading edge has to be balanced by

22   retraction of the tail[1,2] and where multiple protrusions of one cell often compete for

23   dominance, as exemplified in the split pseudopod model of chemotactic migration[3]. The two

24   prevalent models of how remote edges of mammalian cells communicate with each other are

25   based on the sensing of endogenous mechanical parameters that in turn control the

26   actomyosin system. In cell types that tightly adhere to substrates via focal adhesion

27   complexes it has been proposed that actomyosin itself is the sensing structure and that

28   adhesion sites communicate mechanically via actin stress fibers: when contractile stress

29   fibers were pharmacologically, physically or genetically perturbed in mesenchymal cells, the

30   cells lost their coherent shape and spread in an uncontrolled manner[4,5]. While

31   communication via stress fibers is useful for adherent cells, it is unlikely to control the shape

32   of amoeboid cells, which are often loosely or non-adherent and accordingly do not assemble

33   stress fibers[6,7]. A second model suggests that lateral plasma membrane tension, which is

34   thought to rapidly equilibrate across the cell surface, mediates communication between

35   competing protrusions and serves as an input system to control actomyosin dynamics[8-11].

36   However, many amoeboid cells (such as DCs) are large and ramified[12] and particularly when

37   they are tightly embedded in 3D matrices it is questionable whether lateral membrane

38 tension is able to equilibrate across the cell body[13]. Any alternative "internal shape sensor"
39 would need to operate across the cellular scale and mediate communication between cell
40 edges often more than hundred micrometers apart. Centrally nucleated MTs seem ideally
41 suited for this task. We recently found that when leukocytes migrate through complex
42 geometries, their nucleus acts as a mechanical gauge to lead them along the path of least
43 resistance[14]. By spatial association with the nucleus, the MTOC and its nucleated MTs were
44 involved in this navigational task, demonstrating that the positioning of the MTOC relative to
45 the nucleus is critical for amoeboid navigation.

46 As cytoskeletal dynamics are notoriously difficult to visualize *in situ* or in physiological
47 environments like collagen gels we used microfluidic pillar mazes[15] as a reductionist setup
48 that mimics some of the geometrical complexities of interstitial matrices while being
49 accessible to imaging (Supplementary Fig. 1a-c). Within these devices cells are confined
50 between two adjacent surfaces intersected by pillars of variable spacing and exposed to
51 soluble gradients of the chemokine CCL19. CCL19 polarizes and directionally guides DCs and
52 within the organism this leads them via lymphatic vessels towards the center of the draining
53 lymph node[16]. To track MT plus ends we generated precursor cell lines stably expressing end
54 binding protein 3 fused to mCherry (EB3-mCherry) and differentiated them into DCs. During
55 time lapse imaging the MTOC appeared as the brightest spot radiating MT plus ends,
56 indicating that MTs nucleate almost exclusively at the MTOC which is mainly located behind
57 the nucleus (Fig. 1a, Supplementary Fig. 1d-f). When cells navigated through the pillar maze,
58 the MTOC moved in a remarkably straight line up the chemokine gradient although transient
59 lateral protrusions regularly explored alternative paths between the pillars (Fig. 1b). Notably,
60 MT plus ends vanished from lateral protrusions that later became retracted (Supplementary
61 Movie 1). To capture MT dynamics more quantitatively we imaged DCs migrating along
62 chemokine gradients when confined under a pad of agarose[17] where the flattened
63 morphology allows faithful tracing of fluorescent signal (Supplementary Figure 1a, d). Here,
64 cells migrate persistently and are stably segregated into a protruding leading edge and a
65 retracting trailing edge (Fig. 1c). Visualization of the MT binding domain of ensconsin (EMTB)
66 revealed long lived MTs at the leading lamellipodium while MT dynamics were increased at
67 the trailing edge, exhibiting higher frequencies of shrinkage events compared to front
68 directed filaments (Fig. 1d, Supplementary Fig. 1g and Supplementary Movie 2). These
69 observations demonstrate that MT depolymerization is associated with cellular retraction.

70   To test for a causal relationship between MT depolymerization and retraction we devised a

71   photo-pharmacological approach to depolymerize MTs in migratory cells with spatiotemporal

72   control. We used Photostatin-1 (PST-1), a reversibly photo-switchable analogue of

73   combretastatin A-4, which can be functionally toggled between the active and inactive state

74   by blue and green light, respectively[18]. To validate the approach, we locally activated the drug

75   under simultaneous visualization of MT plus ends using EB3-mCherry. We found that local

76   photo-activation triggered almost instantaneous disappearance of the EB3 signal in the

77   presence but not in the absence of Photostatin (Supplementary Fig. 1h), indicating rapid

78   stalling of MT polymerization. Local depolymerization in protruding areas of the cell led to

79   consistent collapse of the illuminated protrusion and subsequent re-polarisation of the cell

80   (Fig. 1e, Supplementary Movie 3). This response was only observed in the presence of

81   Photostatin, while in the absence of the drug cells were refractory to illumination. These data

82   demonstrate a causal relationship between MT depolymerization and cellular retraction. This

83   effect can act locally within a cell, raising the possibility that MTs coordinate subcellular

84   retractions when navigating through geometrically complex environments such as collagen

85   gels or a physiological interstitium.

86   To directly address the impact of the MT cytoskeleton on the coordination of competing

87   protrusions, we used a microfluidic setup in which DCs migrate in a straight channel towards

88   a junction where the channel splits into four paths. In this setup DCs initially insert protrusions

89   into all four channels before they retract all but one protrusion and thereby select one path

90   along which they advance (Figure 2a, Supplementary Figure 1a). Global depletion of MTs

91   using nocodazole (Supplementary Fig. 2a) led to uncoordinated protrusion dynamics and

92   resulted in cell entanglement due to defective retraction of lateral protrusions (Figure 2b).

93   Frequently, cells lost cytoplasmic coherence when competing protrusions continued to

94   migrate up the chemokine gradient until the cell ruptured (Figure 2c, Supplementary Movie

95   4). Similarly, cells migrating *in situ* failed to reach lymphatic vessels (Supplementary Fig. 2b)

96   and cells migrating in collagen gels lost cytoplasmic coherence and fragmented upon

97   nocodazole treatment (Supplementary Fig. 2c, Supplementary Movie 5). In contrast to

98   complex environments such as bifurcating channels and collagen gels, MT depolymerization

99   did not affect cell coherence and general migratory capacity in linear microfluidic channels.

100   In such geometrically simple environments where uniaxial polarity is externally enforced and

101   where there is no competition of multiple protrusions, nocodazole merely caused cells to

102   switch direction more frequently than untreated cells (Fig. 2d, e, Supplementary Movie 6,

103   Supplementary Fig. 2d-g).

104   As demonstrated in other cell types, nocodazole treatment triggered a global increase of

105   RhoA activity and myosin light chain (MLC) phosphorylation[19,20] (Supplementary Fig. 2h, i) and

106   pharmacological inhibition of the effector kinase Rho-associated protein kinase (ROCK) by

107   Y27632 reverted this effect. Accordingly, in linear channels nocodazole-induced directional

108   switching was reverted by additional ROCK inhibition (Fig. 2f-h, Supplementary Movie 6),

109   indicating that an important function of MTs is to both control the activity and to stabilize the

110   localization of the cell's contractile module. As expected, ROCK inhibition failed to rescue cell

111   integrity and locomotion after MT depletion in complex environments (Figure 2i-l,

112   Supplementary Movie 5). Here, contractility is rate limiting for locomotion and ROCK

113   inhibition alone caused the cells to entangle (Fig. 2m). Together our data add evidence that

114   MTs act upstream of the contractile module and that actomyosin contractility is locally

115   coordinated by MT depolymerisation, which effectively coordinates competing protrusions

116   when cells migrate through complex environments.

117   One established molecular link between MT depolymerization and actomyosin contraction is

118   the MT-regulated RhoA guanine nucleotide exchange factor (GEF) Lfc, the murine homologue

119   of GEF-H1[21]. When Lfc is sequestered to MTs it is locked in its inactive state and only upon

120   release from MTs it is targeted to membrane associated sites where it becomes active and

121   triggers actomyosin contraction[22,23]. To test whether Lfc is involved in coordinating

122   protrusions we knocked out *Arhgef2*, the Lfc encoding gene in mice (Supplementary Fig. 3a-

123   f) and placed mature DCs into bifurcating microfluidic channels (Fig. 3a, b, Supplementary Fig.

124   4a). In line with the finding that Lfc mediates between MTs and myosin II (Supplementary Fig.

125   4b, c, d), Lfc^{-/-} DCs showed increased passage times due to defective retraction of

126   supernumerary protrusions (Fig. 3c, d) although showing no differences in MT organization

127   (Supplementary Fig. 4e-g). Similar to nocodazole-treated cells, Lfc^{-/-} DCs often advanced

128   through more than one channel (Fig. 3b), ultimately resulting in auto-fragmentation into

129   migratory cytoplasts (Fig. 3e, Supplementary Movie 7). When DCs migrated in straight

130   channels and even when confronted with single constrictions, Lfc^{-/-} cells passed with the same

131   speed and efficiency as wildtype cells (Fig. 3f, Supplementary Fig. 4h), demonstrating that

132   neither locomotion nor passage through constrictions was perturbed but rather the

133   coordination of competing protrusions. These data indicate that in complex 3D geometries,

5

134   where the cell has to choose between different paths, MTs - via Lfc and myosin II - specify

135   entangled protrusions for retraction.

136   To determine how the Lfc pathway affects the contractile module we dynamically visualized

137   MLC localization in Lfc$^{-/-}$ and wildtype DCs migrating under agarose towards CCL19 gradients.

138   While MLC was largely excluded from the leading lamellipodium, two distinct pools were

139   detectable in the cell body of wildtype cells: one at the trailing edge and one in the cell center,

140   at the base of the lamellipodium and around the nucleus (Fig. 4a, Supplementary Fig. 5a, b).

141   Quantification of the distance between center of mass and center of MLC signal showed that

142   migrating Lfc$^{-/-}$ cells completely lost MLC polarization at the trailing edge, but maintained MLC

143   in the cell center (Fig. 4b-d, Supplementary Fig. 5c, d and Supplementary Movie 8). The same

144   distribution pattern was obtained by determining the localization of the active form of MLC

145   (phospho-MLC) (Fig. 4e) and its effector protein moesin (Supplementary Fig. 5e, f) in fixed

146   samples. This demonstrates that Lfc-deficiency leads to mislocalization of the contractile

147   module and consequently to a loss of myosin II mediated contraction in peripheral

148   protrusions. To address how this impacts overall locomotion, we next measured the

149   migratory capacity of Lfc$^{-/-}$ DCs under physiological conditions. *In situ* migration in explanted

150   ear sheets showed that Lfc$^{-/-}$ cells reached the lymphatic vessels later than control cells (Fig.

151   4f) and chemotaxis of Lfc$^{-/-}$ DCs in collagen gels was substantially impaired (Fig. 4g,

152   Supplementary Movie 9). When we measured cell lengths in 3D collagen gels, Lfc$^{-/-}$ DCs were

153   significantly elongated compared to control cells, indicating retraction defects (Fig. 4h).

154   In cells that employ an amoeboid mode of migration, defective retraction can not only stall

155   locomotion by entanglement but might also lead to failed disassembly of integrin adhesion

156   sites. We therefore tested the role of adhesion-resolution in under agarose assays, where,

157   depending on the surface conditions, DCs can flexibly shift between adhesion-dependent and

158   adhesion-independent locomotion[24]. Under adhesive conditions Lfc$^{-/-}$ DCs were elongated

159   compared to wildtype cells (Fig. 5a) and this elongation was lost when the migratory substrate

160   at the bottom was passivated with polyethylene glycol (PEG) (Fig. 5b, e). When cells on

161   adhesive surfaces were treated with nocodazole, wildtype cells shortened, as expected due

162   to hypercontractility (Fig. 5c). Notably, Lfc$^{-/-}$ DCs elongated even more upon treatment with

163   nocodazole (Fig. 5c, lower panel), indicating that elimination of Lfc-mediated

164   hypercontractility unmasked additional modes of MT-mediated length control. Elongation of

165   Lfc$^{-/-}$ cells by nocodazole was also largely absent on PEG-coated surfaces (Fig. 5d, f,

166   Supplementary Movie 10). Importantly, not only morphological, but also migratory
167   parameters were restored on passivated surfaces (Fig. 5g, h). Together, these data
168   demonstrate that whenever DCs migrate in an adhesion-mediated manner, MTs control de-
169   adhesion and this is partially mediated via Lfc and myosin II. We conclude that MT
170   depolymerization in peripheral regions of migrating DCs locally triggers actomyosin-mediated
171   retraction via the RhoA GEF Lfc. Thereby MTs coordinate protrusion-retraction dynamics and
172   prevent that the cell gets too long or ramified.

173

174   Although it is likely that multiple feedback loops signal between actin and MTs, we show that
175   there is a strong causal link between local MT catastrophes and cellular retraction, with MTs
176   acting upstream. This raises the key question how MT stability is locally regulated in DCs.
177   Among many possible inputs (adhesion, chemotactic signals etc.) one simple option might be
178   related to the fact that in leukocytes the MTOC is the only site where substantial nucleation
179   of MTs occurs. In complex environments (like the pillar maze we devised) the MTOC of a DC
180   moves a remarkably straight path, while lateral protrusions constantly explore the
181   environment (Figure 1b). Hence, passage of the MTOC beyond an obstacle is the decisive
182   event determining the future trajectory of the cell. Upon passage of the MTOC, sheer
183   geometry might determine that all but the leading protrusion are cut off MT supply because
184   MTs are too inflexible to find their way into curved, narrow and ramified spaces. Together,
185   we propose that MTs serve as an internal explorative system of the cell that informs
186   actomyosin whenever a peripheral protrusion locates too distant from the centroid and
187   thereby initiates its retraction.

188

198

199 **Conflict of interest**

200 The authors declare no competing financial interests.

201

202

References

1. Xu, J. *et al.* Divergent signals and cytoskeletal assemblies regulate self-organizing polarity in neutrophils. *Cell* **114,** 201–214 (2003).

2. Tsai, T. Y.-C. *et al.* Efficient Front-Rear Coupling in Neutrophil Chemotaxis by Dynamic Myosin II Localization. *Developmental Cell* **49,** 189–205.e6 (2019).

3. Insall, R. H. Understanding eukaryotic chemotaxis: a pseudopod-centred view. *Nature Publishing Group* **11,** 453–458 (2010).

4. Cai, Y. *et al.* Cytoskeletal coherence requires myosin-IIA contractility. *Journal of Cell Science* **123,** 413–423 (2010).

5. Cai, Y. & Sheetz, M. P. Force propagation across cells: mechanical coherence of dynamic cytoskeletons. *Current Opinion in Cell Biology* **21,** 47–50 (2009).

6. Friedl, P. & Wolf, K. Plasticity of cell migration: a multiscale tuning model. *The Journal of Cell Biology* **188,** 11–19 (2010).

7. Valerius, N. H., Stendahl, O., Hartwig, J. H. & Stossel, T. P. Distribution of actin-binding protein and myosin in polymorphonuclear leukocytes during locomotion and phagocytosis. *Cell* **24,** 195–202 (1981).

8. Diz-Muñoz, A. *et al.* Membrane Tension Acts Through PLD2 and mTORC2 to Limit Actin Network Assembly During Neutrophil Migration. *PLoS Biol.* **14,** e1002474 (2016).

9. Houk, A. R. *et al.* Membrane tension maintains cell polarity by confining signals to the leading edge during neutrophil migration. *Cell* **148,** 175–188 (2012).

10. Keren, K. *et al.* Mechanism of shape determination in motile cells. *Nature* **453,** 475–U1 (2008).

11. Murrell, M., Oakes, P. W., Lenz, M. & Gardel, M. L. Forcing cells into shape: the mechanics of actomyosin contractility. *Nature Publishing Group* **16,** 486–498 (2015).

12. Friedl, P. & Weigelin, B. Interstitial leukocyte migration and immune function. *Nat Immunol* **9,** 960–969 (2008).

13. Shi, Z., Graber, Z. T., Baumgart, T., Stone, H. A. & Cohen, A. E. Cell Membranes Resist Flow. *Cell* (2018). doi:10.1016/j.cell.2018.09.054

14. Renkawitz, J. *et al.* Nuclear positioning facilitates amoeboid migration along the path of least resistance. *Nature* 1–29 (2019). doi:10.1038/s41586-019-1087-5

15. Renkawitz, J., Reversat, A., Leithner, A., Merrin, J. & Sixt, M. Micro-engineered 'pillar forests' to study cell migration in complex but controlled 3D environments. *Methods*

235   *Cell Biol.* **147,** 79–91 (2018).

236 16. Heuzé, M. L. *et al.* Migration of dendritic cells: physical principles, molecular
237   mechanisms, and functional implications. *Immunol Rev* **256,** 240–254 (2013).

238 17. Heit, B. & Kubes, P. Measuring chemotaxis and chemokinesis: the under-agarose cell
239   migration assay. *Sci. STKE* **2003,** PL5–pl5 (2003).

240 18. Borowiak, M. *et al.* Photoswitchable Inhibitors of Microtubule Dynamics Optically
241   Control Mitosis and Cell Death. *Cell* **162,** 403–411 (2015).

242 19. Liu, B. P., Chrzanowska-Wodnicka, M. & Burridge, K. Microtubule depolymerization
243   induces stress fibers, focal adhesions, and DNA synthesis via the GTP-binding protein
244   Rho. *Cell Adhes. Commun.* **5,** 249–255 (1998).

245 20. Takesono, A., Heasman, S. J., Wojciak-Stothard, B., Garg, R. & Ridley, A. J. Microtubules
246   Regulate Migratory Polarity through Rho/ROCK Signaling in T Cells. *PLoS ONE* **5,** e8774–
247   15 (2010).

248 21. Kwan, K. M. & Kirschner, M. W. A microtubule-binding Rho-GEF controls cell
249   morphology during convergentextension of Xenopus laevis. *Development* **132,** 4599–
250   4610 (2005).

251 22. Krendel, M., Zenke, F. T. & Bokoch, G. M. Nucleotide exchange factor GEF-H1 mediates
252   cross-talk between microtubules and the actin cytoskeleton. *Nature Cell Biology* **4,**
253   294–301 (2002).

254 23. Ren, Y., Li, R., Zheng, Y. & Busch, H. Cloning and characterization of GEF-H1, a
255   microtubule-associated guanine nucleotide exchange factor for Rac and Rho GTPases.
256   *Journal of Biological Chemistry* **273,** 34954–34960 (1998).

257 24. Renkawitz, J. *et al.* Adaptive force transmission in amoeboid cell migration. *Nature Cell*
258   *Biology* **11,** 1438–1443 (2009).

259

260

261   **Figure legends**

262   **Figure 1. The microtubule organizing center acts as a pathfinder by coordinating protrusion**

263   **dynamics. a**, DC migrating within a pillar array. Upper panel shows EB3-mCherry expression

264   profile. Lower panel outlines dynamic cell shape changes. Scale bar, 10µm. **b**, Time projection

265   of image sequence shown in **a**. Left panel indicates MTOC position over time. Right panel

266   outlines formation of multiple explorative protrusions over time. **c**, EMTB-mCherry expressing

267   DC migrating under a pad of agarose. Purple box indicates protrusive cell front, whereas grey

268   boxed area denotes contractile trailing edge. **d**, MT dynamics during directed migration.

269   Growth (purple arrowheads) and shrinkage (white arrowheads) frequencies of individual MT

270   filaments (according to EMTB labelling) were assessed in protrusive (front, purple box) vs.

271   contractile (back, grey box) areas of the same migratory cell. Growth events and catastrophes

272   ≥1µm were tracked for n = 10 filaments in the respective region of N = 8 cells. Mean ± S.D.

273   **** $P \leq 0.0001$. Scale bar, 5µm. **e**, Time-lapse sequence of control or PST-1 treated cells,

274   which were locally photo-activated (red box) during migration under agarose (left panels).

275   Middle panels display kymograph analysis of the photo-activated area shown on the left (red

276   line). The time point of photo-activation is shown in red. Right panel: Frequency of local

277   retractions upon photo-activation of control or PST-1 treated DCs during migration (n = 26

278   cells per condition ± S.D. from N = 3 experiments). * $P \leq 0.05$, **** $P \leq 0.0001$.

279

280   **Figure 2. Microtubules coordinate protrusion dynamics via the contractile module. a**, Left

281   panel outlines channel geometry of path choice device. Middle panel: Lifeact-GFP expressing

282   DC migrating within a path choice device of 5µm height. Time projection of signal distribution

283   is shown in right panel. Scale bar, 10µm. **b**, Nocodazole-treated Lifeact-GFP expressing cell

284   migrating within a path choice device. Note that the cell extends elongated protrusions into

285   different channels. Red arrowhead denotes a cell rupturing event during the decision making

286   process. Right panel outlines migratory behavior of cell and cellular fragment over time. **c**,

287   Frequency of cell rupturing events during path choice decision. Control: n = 43 cells;

288   nocodazole: n = 44 cells of N = 2 experiments. **d**, Time lapse sequence of a cell migrating

289   within a linear microchannel of 5µm height. **e**, Nocodazole-treated cell migrating in the same

290   configuration as in **d. f**, Cell treated with a combination of Y27632 plus nocodazole migrating

291   as shown in **d**. Scale bar, 10µm. **g**, Migration speed of control, nocodazole- (Noco.) treated or

292   double-treated (Y./N.) cells using Y27632 and nocodazole within microchannels (n = minimum

11

293 of 74 cells per condition from N = 4 experiments). Boxes extend from 25th to 75th percentile.

294 Whiskers span minimum to maximum values. **** P ≤ 0.0001. **h**, Directionalities of control,

295 nocodazole- (Noco.) treated or double-treated (Y./N.) cells using Y27632 and nocodazole

296 within microchannels (n = minimum of 74 cells per condition from N = 4 experiments). Boxes

297 extend from 25th to 75th percentile. Whiskers span minimum to maximum values. **** P ≤

298 0.0001, **** P ≤ 0.0001. **i**, DCs migrating within a collagen gel either non-treated (control) or

299 double-treated with Y27632 and nocodazole (Y./N.). Note the different time intervals per

300 condition. Red arrowheads indicate loss of cellular coherence in the double-treated cell. Scale

301 bars, 10μm. **j**, Automated analysis of y-directed speed of non-treated, nocodazole-treated

302 (Noco.) or double-treated cells using Y27632 and nocodazole (Y./N.). Plot shows mean

303 migration velocities over time ± S.D. from N = 4 experiments. **k**, Lifeact-GFP expressing DC

304 double-treated with Y27632 plus nocodazole (Y./N.) migrating as in **a**. Red arrowhead denotes

305 a cell rupturing event during the decision making process. Right panel outlines migratory

306 behavior of cell and cellular fragment over time. **l**, Frequency of cell rupturing events during

307 path choice decision. Control: n = 40 cells; Y./N. : n = 80 cells of N = 2 experiments. **m**, Lifeact-

308 GFP expressing DC treated with Y27632 migrating as in **a**. Note the extended protrusions

309 reaching far into separate channels without generating a productive decision within the

310 indicated time. Time projection of signal distribution is shown in right panel.

311

312 **Figure 3. Microtubules mediate retraction of supernumerary protrusions via Lfc. a**, Time

313 lapse sequence of a wildtype littermate control cell migrating within a path choice device.

314 Scale bar, 10μm. **b**, Time lapse sequence of a $Lfc^{-/-}$ cell migrating within a path choice device.

315 Red arrowheads denote multiple rupturing events of a single cell. Scale bar, 10μm. **c**, Junction

316 point passing times of $Lfc^{+/+}$ (n = 79 cells of N = 3 experiments) and $Lfc^{-/-}$ (n = 49 cells of N = 2

317 experiments) DCs. Boxes extend from 25th to 75th percentile. Whiskers span minimum to

318 maximum values. *** P ≤ 0.001. **d**, Junction point passing times depending on presence of

319 single non-competing or multiple competing protrusions per cell of $Lfc^{+/+}$ (n = 37 cells of N =

320 3 experiments) and $Lfc^{-/-}$ (n = 46 cells of N = 2 experiments) DCs. Boxes extend from 25th to

321 75th percentile. Whiskers span minimum to maximum values. ** P ≤ 0.01. **e**, Frequency of cell

322 rupturing events during path-choice decision of $Lfc^{+/+}$ (n = 79 cells ± S.D. of N = 3 experiments)

323 and $Lfc^{-/-}$ (n = 52 cells ± S.D. of N = 2 experiments) DCs. **f**, Migration of DCs within straight,

324 single constriction-containing microchannels. Graphs show constriction point passing times

325   of Lfc$^{+/+}$ (n = 114 cells of N = 3 experiments) and Lfc$^{-/-}$ (n = 195 cells of N = 3 experiments) DCs.

326   Boxes extend from 25th to 75th percentile. Whiskers span minimum to maximum values.

327

328   **Figure 4. Lfc-dependent myosin accumulation controls cellular locomotion. a**, A myosin light

329   chain-GFP (MLC-GFP) expressing DC migrating under agarose along a soluble CCL19 gradient.

330   Central- (orange box) and peripheral- (purple box) MLC accumulation is outlined. Scale bar,

331   10μm. MLC accumulation during migration under agarose in **(b)** wildtype- or **(c)** Lfc$^{-/-}$ cells.

332   Scale bar, 10μm. Middle panels indicate cell shapes over time. Right panels indicate mean

333   MLC fluorescence distribution along the anterior-posterior polarization axis (dashed line) in

334   80sec intervals. **d**, Localization of MLC accumulation during directed migration of Lfc$^{+/+}$ (red)

335   and Lfc$^{-/-}$ (blue) DCs. To account for differences in cell length the distance between cell center

336   and MLC accumulation was normalized to cell length. Graph shows distance of n = 7 migratory

337   cells per condition ± S.D. **e**, Localization of endogenous phospho-MLC(S19) in fixed migratory

338   DCs (left panel). Right panel indicates position of MLC accumulation relative to cell length of

339   n = 16 cells per condition from N = 4 experiments. Boxes extend from 25th to 75th percentile.

340   Whiskers span minimum to maximum values. **** $P \leq 0.0001$. Scale bar, 10μm. **f**, *In situ*

341   migration of exogenous DCs on a mouse ear sheet. Lymphatic vessels were stained for Lyve-

342   1, DCs with TAMRA respectively. Right panel indicates the mean distance of cells from

343   lymphatic vessels. Per experiment two mouse ears with two fields of view were analyzed of

344   N = 4 experiments. Boxes extend from 25th to 75th percentile. Whiskers span minimum to

345   maximum values. * $P \leq 0.05$. Scale bar, 100μm. **g**, Automated analysis of y-directed migration

346   speed within a collagen network along soluble CCL19 gradient. Plot shows mean migration

347   velocities over time ± S.D. from N = 7 experiments. **h**, Upper panels: Cell outlines of Lfc$^{+/+}$ (left)

348   and Lfc$^{-/-}$ (right) DCs migrating within a collagen network along a soluble CCL19 gradient. Scale

349   bar, 10μm. Lower panel shows lengths of cells migrating within a collagen network of n = 85

350   individual cells per condition from N = 4 experiments. Boxes extend from 25th to 75th

351   percentile. Whiskers span minimum to maximum values. *** $P \leq 0.001$.

352

353   **Figure 5. Lfc regulates microtubule-mediated adhesion resolution.** Cell shape outlines of

354   non-treated control cells migrating under agarose under adhesive **(a)** or repellent (PEG

355   coated) **(b)** conditions. Cell shape outlines of nocodazole-treated cells migrating under

356   agarose under adhesive **(c)** or repellent (PEG coated) **(d)** conditions. Upper panels show

357 littermate control wildtype cells, lower panels show Lfc$^{-/-}$ cells. Scale bars, 10μm. **e**, Cell

358 lengths of non-treated control cells migrating under adhesive and repellent conditions (n =

359 minimum of 80 cells per condition from N = 5 experiments). Boxes extend from 25th to 75th

360 percentile. Whiskers span minimum to maximum values. **** P ≤ 0.0001. **f**, Cell lengths of

361 nocodazole-treated cells migrating under adhesive and repellent conditions (n = minimum of

362 80 cells per condition from N = 5 experiments). Boxes extend from 25th to 75th percentile.

363 Whiskers span minimum to maximum values. **** P ≤ 0.0001. **g**, Migration distance of Lfc$^{+/+}$

364 and Lfc$^{-/-}$ DCs migrating under agarose under non-adhesive (PEG coated) conditions of n =

365 minimum of 80 cells per condition from N = 5 experiments. Cells were either non-treated or

366 treated with nocodazole. Boxes extend from 25th to 75th percentile. Whiskers span minimum

367 to maximum values. * P ≤ 0.05, **** P ≤ 0.0001. **h**, Directionalities of Lfc$^{+/+}$ and Lfc$^{-/-}$ DCs

368 migrating under agarose under non-adhesive conditions (PEG). Cells were either non-treated

369 or nocodazole- treated (n = minimum of 80 cells per condition from N = 5 experiments). Boxes

370 extend from 25th to 75th percentile. Whiskers span minimum to maximum values. **** P ≤

371 0.0001.

372

373

374 **Materials and Methods**

375 **Mice**

376 All mice used in this study were bred on a C57BL/6J background and maintained at the

377 institutional animal facility in accordance with the IST Austria ethics commission in

378 accordance with the Austrian law for animal experimentation. Permission of all experimental

379 procedures was granted and approved by the Austrian federal ministry of science, research

380 and economy (identification code: BMWF-66.018/0005-II/3b/2012).

381 **Generation of Lfc$^{-/-}$ mice**

382 A cosmid containing the full genomic sequence of the gene that encodes Lfc (*Arhgef2*) was

383 isolated from a 129 mouse genomic library with Lfc cDNA probes (106-630, 631-1057 and

384 1060-1478 bp) amplified by RT-PCR. The genomic DNA region between base pairs 1193-1477,

385 coding for amino acids 351-445 in the DH domain and DH/PH domain interface was

386 exchanged for a neomycin cassette flanked by LoxP sites. The targeting construct was

387 linearized with *Not*I and electroporated into R1 ES cells. Homologous recombinants were

388 selected in the presence of G418 (150 µg/ml) and gancyclovir (2 µM) and analyzed by

389 Southern blotting. Positive embryonic stem cell clones were aggregated with eight cell-stage

390 mouse embryos to generate chimeras. The resulting mice were genotyped by Southern blot

391 and PCR. Primers (5'– CGGGGATCCATTCGGTTGTAA –3') and (5'– AAGCGGCATGGAGTTCAGGA

392 –3') amplified a 365-bp fragment specific for the wild type allele, whereas primers (5'–

393 AGAGTTCTGCAGCCGCCACACCA–3') and 5'–GGTGGGGGTGGGGTGGGATTAGATA –3')

394 amplified a 500-bp fragment specific for the targeted allele. We refer to these mice as Lfc$^{-/-}$

395 mice throughout the entire manuscript. Western blot analysis using a Lfc-specific antibody

396 was performed to confirm that Lfc$^{-/-}$ mice had no expression of Lfc protein. Mice were

397 backcrossed to C57BL/6 background for more than 12 generations. Dendritic cells were

398 generated from bone marrow isolated from littermates or age-matched wildtype and Lfc$^{-/-}$ 8-

399 12 week-old mice. Mice were bred and housed in accordance with institutional guidelines.

400

401 **Generation of immortalized hematopoietic progenitor reporter cell lines**

402 Hematopoietic progenitor cell lines were generated by retroviral delivery of an estrogen-

403 regulated form of HoxB8 as described recently [25,26]. Briefly, bone marrow of 6-12 week of

404    $Lfc^{+/+}$ and $Lfc^{-/-}$ mice was isolated and retrovirally transduced with an estrogen-regulated form

405   of the HoxB8 transcription factor. After expansion of immortalized cells, lentiviral spin

406   infection (1500g, 1h) was carried out in the presence of 8µg/ml Polybrene and the lentivirus

407   coding for fluorescent expression construct of interest. Following transduction, cells were

408   selected for stable virus insertion using 10µg/ml Blasticidin for at least one week. Cells

409   expressing fluorescent reporter constructs were sorted using fluorescence-activated cell

410   sorting (FACS Aria III, BD Biosciences) prior to migration experiments.

411

412   **Dendritic cell culture**

413   Culture was started either from freshly isolated bone marrow of 6-12 week old mice with

414   C57BL/6J background (wildtype, $Lfc^{-/-}$, or Lifeact-GFP[27] as described earlier[28] or from stable

415   hematopoietic progenitor cell lines after washing out estrogen. DC differentiation was

416   induced by plating $2x10^6$ cells (bone marrow) or $2x10^5$ cells (progenitor cells) in complete

417   media (RPMI 1640 supplemented with 10% Fetal Calf Serum, 2mM L-Glutamine, 100U/ml

418   Penicillin, 100µg/ml Streptomycin, 50µM ß-Mercaptoethanol) (all purchased from Invitrogen)

419   containing 10% Granulocyte-Monocyte colony stimulating factor (GM-CSF, supernatant from

420   hybridoma culture). To induce maturation, cells were stimulated overnight with 200ng/ml

421   Lipopolysaccharide from *E.coli* 0127:B8 (Sigma) and used for experiments on days 9-10.

422

423   *In situ* **migration assay**

424   Six to eight weeks old female C57BL/6J mice were sacrificed and individual ear sheets

425   separated into dorsal and ventral halves as described previously[29]. Cartilage free ventral

426   halves were incubated for 48h at 37°C, 5% CO_2 with ventral side facing down in a well plate

427   filled with complete medium. The medium was changed once 24h post-incubation-start. If

428   indicated, pharmacological inhibitors were added to the medium. Ear sheets were fixed with

429   1% PFA followed by immersion in 0.2% Triton X-100 in PBS for 15min and three washing steps

430   á 10min with PBS. Unspecific binding was prevented by 60min incubation in 1%BSA in PBS at

431   room temperature. Incubation with primary rat-polyclonal antibody against LYVE-1 in

432   combination with rat-polyclonal biotinylated anti-MHC-II antibody (both R&D Systems) was

433   done for 2h at room temperature. After three times 10min washing with 1% BSA in PBS

434   consecutive incubation using Alexa Fluor 488-AffiniPure F(ab')$_2$ fragment donkey anti-rat IgG

435   (H+L) secondary antibody and streptavidin-Cy3 secondary antibody (both Jackson

16

436 ImmunoResearch) was done. Samples were incubated 45min in first secondary antibody in

437 the dark followed by 10min washing in 1% BSA in PBS and subsequent incubation with second

438 secondary antibody. Samples mounted with ventral side up on a microscope slide, protected

439 with a coverslip and stored at 4˚C in the dark.

440 In order to determine the distance between the lymphatic vessels and DCs a mask was

441 created by manually outlining lymphatic vessels depending on Lyve-1 staining and segmenting

442 cells according to their fluorescence intensity. The distance between cells and lymphatic

443 vessels was quantified using a custom-made Matlab script, which determines the closest

444 distance from the segmented cells to the border of the lymphatic vessel binary image. Image

445 borders were excluded from analysis.

446

447 ***In vitro* collagen gel migration assay**

448 Custom made migration chambers were assembled by using a plastic dish containing a 17mm

449 hole in the middle, which was covered by coverslips on each side of the hole. Three-

450 dimensional scaffolds consisting of 1.73mg/ml bovine Collagen I were reconstituted *in vitro*

451 by mixing $3x10^5$ cells in suspension with Collagen I suspension buffered to physiological pH

452 with Minimum Essential Medium and Sodium Bicarbonate in a 1:2 ratio. To allow

453 polymerization of Collagen fibers, gels were incubated 1h at 37˚C, 5% CO_2. Directional cell

454 migration was induced by overlaying the polymerized gels with 0.63µg/ml CCL19 diluted in

455 complete media (R&D Systems). To prevent drying-out of the gels, migration chambers were

456 sealed with Paraplast X-tra (Sigma-Aldrich). The acquisition was performed in 60sec intervals

457 for five hours at 37˚C, 5% CO_2. Detailed description of experimental procedure can be found

458 elsewhere[30].

459

460 **Analysis of y-displacement**

461 Quantification of y-directed migration analysis of cell population was performed as described

462 earlier [31]. Briefly, raw data image sequences were background corrected and particles smaller

463 and bigger than an average cell were excluded. For each time point the lateral displacement

464 in y-direction was determined with the previous frame to generate the best overlap, which

465 yields the y-directed migration velocity of a cell population.

466

467 **Migration within micro-fabricated polydimethylsiloxane (PDMS) based devices.**

17

468 Generation of PDMS-based devices and detailed experimental protocols can be found

469 elsewhere[15,31]. Briefly, photomasks were designed using Coreldraw X18, printed on a

470 photomask (5" square quartz, 1μm resolution, JD Photo data), followed by a spin coating step

471 using SU-8 2005 (3000 RPM, 30sec, Microchem, USA) and a prebake of 2 min at 95˚C. The

472 wafer was then exposed to ultra-violet light ($90 - 105$ mJ/cm^2 on an EVG mask aligner). After

473 a post-exposure bake of 3 min 95˚C, the wafer was developed in PGMEA. A one-hour

474 silanization with Trichloro(1H,1H,2H,2H-perfluorooctyl)silane was applied to the wafer. The

475 devices were made with a 1:10 mixture of Sylgard 184 (Dow Corning). Air bubbles were

476 removed with a desiccator. The PDMS was cured overnight at 85˚C. Micro-devices were

477 attached to ethanol cleaned coverslips after plasma cleaning for 1h at 85˚C. Before

478 introduction of cells, devices were flushed and incubated with complete medium for at least

479 1h. To visualize the chemokine gradient, similar sized fluorescent dextran conjugated to

480 fluorescinisothiocyanate (FITC) was added to the chemokine solution (200μg/ml, 10kDa,

481 Sigma) due to exhibiting similar diffusion characteristics[32].

482

483 ***In vitro* under-agarose migration assay**

484 To obtain humid migration chambers a 17mm plastic ring was attached to a glass bottom dish

485 using Paraplast X-tra (Sigma-Aldrich) to seal attachment site. For under-agarose migration

486 assay, 4% Ultra Pure Agarose (Invitrogen) in nuclease-free water (Gibco) was mixed with

487 phenol-free RPMI-1640 (Gibco) supplemented with 20% FCS, 1x Hanks buffered salt solution

488 pH 7.3 in a 1:3 ratio. Ascorbic acid was added to final concentration of 50μM and a total

489 volume of 500μl agarose-mix was cast into each migration chamber. After polymerization, a

490 2mm hole was punched into the agarose pad and 2.5μg/ml CCL19 (R&D Systems) was placed

491 into the hole to generate a soluble chemokine gradient. Outer parts of the dish were filled

492 with water followed by 30-minute equilibration at 37˚C, 5% CO_2. The cell suspension was

493 injected under agarose opposite of the chemokine hole to confine DCs between coverslip and

494 agarose. Prior to acquisition, dishes were incubated at least two hours at 37˚C, 5% CO_2 to

495 allow recovery and persistent migration of cells. During acquisition, dishes were held under

496 physiological conditions at 37˚C and 5% CO_2.

497

498 **Immunofluorescence**

499   For fixation experiments a round shaped coverslip was placed in glass bottom dish before

500   casting of agarose and injection of cells. Migrating cells were fixed by adding prewarmed 4%

501   Para-Formaldehyde (PFA) diluted in cytoskeleton Buffer pH6.1 (10mM MES, 150mM NaCl,

502   5mM EGTA, 5mM Glucose, 5mM MgCl$_2$) directly on top of the agarose. After fixation, agarose

503   pad was carefully removed using a coverslip-tweezer followed by 20min incubation of the

504   coverslip in 0.5% Triton X-100 in PBS and three subsequent washing steps á 10min with Tris-

505   buffered saline (TBS) containing 0.1% Tween-20 (Sigma). Samples were blocked to prevent

506   unspecific binding by incubating 60min in blocking solution (5% BSA, 0.1% Tween-20 in TBS).

507   Immunostainings were carried out consecutively by 2h incubation with rat monoclonal anti-

508   alpha-tubulin (AbD serotec), mouse anti-phospho-Myosin light chain 2 (S19) (Cell signaling),

509   mouse anti-gamma tubulin (Sigma) or rabbit anti-acetylated alpha-tubulin (Sigma). Followed

510   by 3x10min washing with blocking solution and 30min incubation using Alexa Fluor® 488-

511   AffiniPure F(ab')$_2$ or Alexa Fluor® 647-AffiniPure F(ab')$_2$ Fragment IgG (H+L) (both Jackson

512   Immuno) secondary antibodies. After incubation washing was done at least three times á

513   5min. Samples were conserved in non-hardening mounting medium with DAPI

514   (VectorLaboratories) and stored at 4˚C in the dark.

515

516   **Immunodetection of whole cell lysates**

517    $3x10^5$ cells were serum starved for 1h followed by drug treatment. After harvesting, cell pellet

518   was snap frozen and lysed using RIPA buffer (Cell Signaling) to which 1mM

519   Phenylmethylsulfonylfluoride was added prior to usage. Samples were supplemented with

520   LDS Sample Buffer and Reducing agent (both Invitrogen) and incubated for 5min at 90˚C

521   before loading on pre-cast 4-12% Bis-Tris acrylamide gel (Invitrogen). Subsequently, samples

522   were transferred to Nitrocellulose membrane using iBlot system (Invitrogen) and blocked for

523   1h in 5% bovine serum albumin in TBS containing 0.01% Tween-20. For whole cell lysate

524   protein detection following antibodies were used: rabbit anti phospho-Myosin Light Chain 2

525   (S19) (1:500), rabbit anti Myosin Light Chain 2 (1:500), rabbit anti GEF-H1 (the mammalian

526   homologue of Lfc) (1:500), rabbit anti phospho-ERM (1:500), rabbit anti ERM (1:500, all Cell

527   Signaling), mouse anti glyceraldehyde 3-phosphate dehydrogenase (GAPDH) (1:1000,

528   BioRad). As secondary antibodies Horseradish Peroxidase (HRP) Conjugated Anti-rabbit and

529   anti-mouse IgG (H + L) antibodies were used in 1:5000 dilutions and enzymatic reaction was

530   started by addition of chemoluminescent substrate for HRP (Super Signal West Femto).

19

531 Chemoluminescence was acquired using a VersaDoc imaging system (BioRad). Western blot

532 signals were quantified manually by normalization to input values and subsequent

533 comparison of each treatment to signal intensity of steady-state level (i.e. control sample).

534

Flow cytometry

536 Before staining, 1-2x10^6 cells were incubated for 15 min at +4°C with blocking buffer (1xPBS,

537 1% BSA, 2mM EDTA) containing 5mg/ml α-CD16/CD32 (2.4G2, BD Biosciences). For surface

538 staining, cells were incubated for 30 min at 37°C with conjugated monoclonal antibodies

539 (mAbs; mouse α-CCR7-PE (4B12), rat α-mouse I-A/I-E-eFluor450 (M5/114.15.2), hamster α-

540 mouse CD11c-APC (N418) diluted at the recommended concentration in blocking buffer. Flow

541 cytometry analysis was performed on a FACS CANTO II flow cytometer (BD Biosciences).

542

Pharmacological inhibitors

544 For perturbation of cytoskeletal and myosin dynamics we used final concentrations of 300nM

545 Nocodazole and 10µM Y27632 (all purchased from Sigma Aldrich). Nocodazole was dissolved

546 in dimethylsulfoxide (DMSO; Sigma Aldrich) and Y27632 in poly-buffered saline. Control

547 samples were usually treated with 1:1000 DMSO if not indicated differentially.

548

Fluorescent reporter constructs

550 Generation of a C-terminal eGFP fusion construct of Lfc was carried out by amplifying Lfc from

551 DC   cDNA   using   a   NotI   restriction   site   containing   forward   (5'

552 ATATGCGGCCGCAATCTCGGATCGAATCCCTCACTCGCG   3')   and   reverse   (5'

553 ATATGCGGCCGCTTAGCTCTCTGAAGCTGTGGGCTCC 3') primer pair. After NotI digestion, Lfc

554 was cloned into a pcDNA3.1 backbone containing eGFP (Express Link™ T4 DNA-Ligase).

555 Correct sequence and orientation of clones was verified by sequencing (Eurofins). The

556 fluorescent plasmid DNA reporter construct coding for EB3-GFP was a kind gift of V. Small

557 (IMBA, Austria). M. Olson (Beatson Institute) generously provided MLC constructs (either

558 fused to eGFP or RFP)[33] and EMTB-3xmCherry constructs were a kind gift of (W. M. Bement,

559 University of Wisconsin)[34]. Gateway cloning technology™ was employed to generate

560 lentivirus from plasmid DNA constructs. Briefly, corresponding DNA segments were amplified

561 using primers containing overhangs with *att*B1 and *att*B2 recombination sites on the 3'- and

562 the 5'-end respectively. In order to obtain an EMTB fusion construct carrying a single mCherry

20

563 tag, the PCR product was size separated via gel electrophoresis and only the fragment of

564 corresponding size (EMTB: 816bp, mCherry: 705bp) was further processed. Gel purified PCR

565 fragments were inserted into pcDNA221 entry vectors (Invitrogen) via BP recombination

566 reaction, generating the entry clone. Expression clones were obtained by carrying out the LR

567 recombination reaction between entry clone and pLenti6.3 destination vector (Invitrogen).

568 Lentivirus production was carried out by co-transfecting LX-293 cells (Chemicon) with the

569 expression clone of interest in conjunction with pdelta8.9 (packaging plasmid) and pCMV-

570 VSV-G (envelope plasmid) (plasmids were a gift from Bob Weinberg)[35]. The supernatant of

571 virus-producing cells was harvested 72h after transfection, snap frozen and stored at -80˚C

572 after sterile filtration.

573

574 **Transgene delivery**

575 To induce expression of fluorescently labeled proteins DCs were transfected according to

576 manufacturer guidelines using nucleofector kit for primary T cells (Amaxa, Lonza Group).

577 Briefly, 5×10^6 were resuspended in 100µl reconstituted nucleofector solution, transferred to

578 an electroporation cuvette and a total amount of 4µg plasmid DNA was added. Cells were

579 transfected by using a protocol specifically designed for electroporating immature mouse DCs

580 (program X-001). After transfection, cells were cultured in 60mm cell culture dishes in

581 complete media and taken for experiments 24h post-transfection. Due to low transfection

582 efficiency of primary cells, transfected cells were FACS sorted prior to experiment using FACS

583 Aria III (BD Biosciences).

584

585 **Luminometric RhoA activity assay**

586 RhoA activities were determined using G-LISA[TM] RhoA Activation Assay Biochem Kit[TM]

587 (Cytoskeleton) according to the manufacturer's instructions. Briefly, 4×10^5 mature BMDCs

588 were lysed in 70µl RIPA buffer (Cell Signaling) and protein concentration determined using

589 the Precision Red[TM] Advanced Protein Assay Reagent (Cytoskeleton). Respective samples

590 were treated with 300nM Nocodazole for 15 min before lysis. All samples were adjusted to a

591 final protein concentration of 0.5mg/ml. Luminescence signals were measured using a

592 microplate photometer at 600nm. Wells containing lysis buffer only were used as reference

593 blanks in all experiments.

594

Microscopy

During all live cell imaging experiments cells were held under physiological conditions at 37˚C, 5% CO_2 in a humidified chamber. Low magnification bright field or DIC time-lapse acquisition was carried out using inverted routine microscopes (Leica), equipped with PAL cameras (Prosilica, Brunaby, BC) controlled by SVS-Visitek software (Seefeld, Germany) using 4x, 10x, 20x objectives or an inverted Nikon Eclipse widefield microscope using a C-Apochromat 20x/0.5 PH1 air equipped with a Lumencor light engine (wavelengths [nm]: 390, 475, 542/575). For high magnification live cell acquisition, either an Andor spinning disc confocal scanhead installed on an inverted Axio observer microscope (Zeiss), using a C-Apochromat 63x/1.2 W Korr UV-VIS-IR objective, or a total internal reflection (TIRF) setup consisting of an inverted Axio observer microscope (Zeiss), a TIRF 488/561 nm laser system (Visitron systems) and an Evolve^{TM} EMCCD camera (Photometrics) triggered by VisiView software (Visitron) was chosen. Photo-activation experiments were conducted on an inverted Spinning disc microscope (iMic) using a 60x/1.35 Oil objective. TAMRA stained DCs were either untreated or treated with 10μM PST-1 in the dark and recorded using a 561nm laser line in 2-second intervals. Photoactivation was carried out on directionally migrating cells using a 405 nm laser line (pixel dwell time: 10 ms, interval: 40 sec). FRAP calibration was carried out on separate samples before each experiment. Acquisition of fixed samples (*in situ* ear crawl in and immunofluorescence samples) was carried out using an upright confocal microscope (LSM700, Zeiss) equipped with a Plan-Apochromat 20x/1.0 W DIC (UV) VIS-IR or a Plan-Apochromat 63x/1.4 Oil objective.

Statistics

All boxes in Box-Whisker plots boxes extend from 25th to 75th percentile and whiskers span minimum to maximum values. Graphs represent pooled data of several cells (n) from independent biological experiments (N) as mentioned in the figure legends. Individual experiments were validated separately and only pooled if showing the same trend. For representation of frequencies, bar charts depict mean values from several independent biological experiments (N) ± S.D. Statistical analysis was conducted out using GraphPad Prism.

Supplementary References

25. Redecke, V. *et al.* Hematopoietic progenitor cell lines with myeloid and lymphoid

22

627   potential. *Nat Meth* 1–13 (2013). doi:10.1038/nmeth.2510

628   26.   Leithner, A. *et al.* Fast and efficient genetic engineering of hematopoietic precursor

629   cells for the study of dendritic cell migration. *Eur. J. Immunol.* **48,** 1074–1077 (2018).

630   27.   Riedl, J. *et al.* Lifeact mice for studying F-actin dynamics. *Nat Meth* **7,** 168–169 (2010).

631   28.   Lutz, M. B. *et al.* An advanced culture method for generating large quantities of highly

632   pure dendritic cells from mouse bone marrow. *Journal of Immunological Methods* **223,**

633   77–92 (1999).

634   29.   Pflicke, H. & Sixt, M. Preformed portals facilitate dendritic cell entry into afferent

635   lymphatic vessels. *Journal of Experimental Medicine* **206,** 2925–2935 (2009).

636   30.   Sixt, M. & Lämmermann, T. In vitro analysis of chemotactic leukocyte migration in 3D

637   environments. *Methods Mol. Biol.* **769,** 149–165 (2011).

638   31.   Leithner, A. *et al.* Diversified actin protrusions promote environmental exploration but

639   are dispensable for locomotion of leukocytes. *Nature Cell Biology* **18,** 1253–1259

640   (2016).

641   32.   Schwarz, J. *et al.* A microfluidic device for measuring cell migration towards substrate-

642   bound and soluble chemokine gradients. *Sci Rep* **6,** (2016).

643   33.   Croft, D. R. *et al.* Actin-myosin-based contraction is responsible for apoptotic nuclear

644   disintegration. *The Journal of Cell Biology* **168,** 245–255 (2005).

645   34.   Miller, A. L. & Bement, W. M. Regulation of cytokinesis by Rho GTPase flux. *Nature Cell*

646   *Biology* **11,** 71–U137 (2009).

647   35.   Stewart, S. A. *et al.* Lentivirus-delivered stable gene silencing by RNAi in primary cells.

648   *RNA* **9,** 493–501 (2003).

649

650 **Supplementary Figure 1. DC migration within diverse matrices to study the role of the MT**

651 **cytoskeleton during cell migration. a**, Schematic representation of migration assays used in

652 this study. Assays range from highly complex (top) and relatively uncontrollable geometries

653 to very simple and precisely controllable PDMS-based structures (bottom). Complexity of the

654 geometrical confinement correlates with dynamic shape changes of cells. Upward-facing

655 arrows indicate high geometrical complexity and cell shape changes respectively. Downward-

656 facing arrows indicate low complexity. **b**, Cell shape changes of a DC migrating in a collagen

657 matrix along a soluble CCL19 gradient. **c**, Dynamic cell shape changes are recapitulated during

658 migration within a defined array of PDMS-based pillar structures. **d**, Left panel: Cells migrating

659 under agarose display a protrusive lamellipodium (lower panel: montage of boxed area)

660 followed by a contractile trailing edge. Scale bar, 10µm. Middle panel: EB3-mCherry localizes

661 to the plus tips of tubulin-GFP decorated MT filaments. Shown is a double-reporter DC

662 migrating under agarose along a soluble CCL19 gradient. Scale bar, 10µm. Right panel: EB3-

663 mCherry faithfully tracks growing MT filaments during DC migration. White arrowhead

664 highlight the localization of EB3 signal at the tip of polymerizing tubulin filaments as the cell

665 advances. Scale bar 5µm. **e**, MT nucleation from centrosomal origin determined by alpha- and

666 gamma-tubulin staining. Right panel shows line scan of signal intensities along purple line in

667 merged image. Scale bar, 10µm. **f**, Determination of MTOC position by alpha- and gamma-

668 tubulin staining with respect to the nucleus. Mean ± S.D. of n = 256 cells from N = 3

669 experiments. **g**, Time-course analysis of MT filament dynamics of migrating DCs expressing

670 EMTB-mCherry. Upper panel indicates leading edge area. The purple arrow represents

671 membrane protrusion and the purple arrowheads represent elongating MT filaments. Lower

672 panel indicates trailing edge area in which black arrow represents membrane retraction and

673 black arrowheads MT filament depolymerization. Red dashed line indicates cell edges. Scale

674 bar, 10µm. **h**, EB3-mCherry localization of control or PST-1 treated cells migrating under

675 agarose along a soluble CCL19 gradient. The red box indicates photo-activated area magnified

676 on the right. Magnified regions show time projection of EB3-mCherry intensities after local

677 photo-activation. Lower panel indicates fluorescence intensity evolution upon photo-

678 activation of control or PST-1 treated cells. The red line highlights the time point of initial

679 photo-activation. Purple arrows indicate the direction of cell migration.

680

681 **Supplementary Figure 2. Perturbation of the MT cytoskeleton affects DCs migration on**

682 **multiple levels. a**, Non-treated control or nocodazole-treated cells migrating under agarose

683 towards a CCL19 gradient were fixed and stained for endogenous distribution of alpha-tubulin

684 and F-actin. Scale bar 10µm. **b**, *In situ* migration of endogenous DCs on a mouse ear sheet. Z-

685 projections of separated ear sheets upon control conditions or nocodazole treatment.

686 Lymphatic vessels were stained for Lyve-1, DCs for MHC-II. Mean distance from lymphatic

687 vessels of endogenous DCs was determined 48h after ear separation (right panel). Per

688 condition, four mouse ears with two fields of view were analyzed. Boxes extend from 25th to

689 75th percentile. Whiskers span minimum to maximum values. ** P ≤ 0.01. Scale bar, 100µm.

690 **c**, Nocodazole-treated DC migrating in a collagen gel towards a soluble CCL19 gradient. Yellow

691 line outlines cell shape. Red arrowheads indicate loss of cellular coherence. Scale bar, 100µm.

692 **d**, Individual cell migration trajectories of cells migrating under agarose upon control

693 conditions and nocodazole treatment of n = 58 cells (Control) and n = 52 cells (Noco.) from N

694 = 4 experiments. **e**, Individual cell outlines over time upon control or nocodazole-treated

695 conditions. Note the stable polarization of control cells contrasting the oscillatory protrusion

696 dynamics of nocodazole-treated cells. **f**, Directionality during migration under agarose of n =

697 50 cells per condition from N = 4 experiments was assessed by comparing accumulated- with

698 euclidean-distance of manually tracked cell trajectories. Boxes extend from 25th to 75th

699 percentile. Whiskers span minimum to maximum values **** P ≤ 0.0001. **g**, Migration speed

700 during migration under agarose along a soluble CCL19 gradient upon control conditions and

701 nocodazole treatment of n = 50 cells per condition from N = 4 experiments. Boxes extend

702 from 25th to 75th percentile. Whiskers span minimum to maximum values. **h**, Levels of active

703 RhoA upon MT depolymerization with nocodazole determined by luminometry. RhoA activity

704 levels were normalized to nocodazole-treated samples. Plotted is mean ± S.D. from N = 3

705 experiments. **** P ≤ 0.0001. **i**, Levels of MLC phosphorylation determined by Western Blot

706 analysis. Cells were treated with the indicated compounds (DMSO, nocodazole or Y27632

707 together with nocodazole (Y./N.)). Mean fluorescence intensity of pMLC was normalized to

708 GAPDH signal and shown as fold increase relative to DMSO control ± S.D in right panel. Blots

709 are representative of N = 3 experiments.

710

711 **Supplementary Figure 3. Generation of a Lfc$^{-/-}$ mouse line. a**, Integration of the Lfc targeting

712 vector into genomic locus. Black boxes represent exons. The neo-lox P cassette was cloned in

25

713 reverse orientation into two, replacing a *SmaI-XhoI* segment. Locations of primers used for

714 PCR are indicated with triangles. Probes A and B were used for Southern blot detection of

715 short and long arms, respectively. S, *Sma*I; Xh, *Xho*I; X*, Xba*I: N, *Nhe*I. **b**, Southern blot analysis.

716 Genomic DNA from Lfc$^{+/+}$, Lfc$^{+/-}$ and Lfc$^{-/-}$ mice was digested with *Xba*I and hybridized with

717 probes B (left panel) and genomic DNA from Lfc$^{+/+}$ and Lfc$^{+/-}$ embryonic stem cells were

718 hybridized with probe A (right panel). **c**, PCR analysis of tail DNA from Lfc$^{+/+}$, Lfc$^{+/-}$ and Lfc$^{-/-}$

719 mice. Locations of primers used for PCR are indicated with triangles in **a**. **d**, Immunoblot

720 analysis of total thymus cell lysates probed for Lfc protein content. **e**, Cell morphologies of

721 immature (NT) and mature (+LPS) Lfc wildtype (upper-lane) and Lfc-deficient (lower-lane)

722 littermate DCs. Note the presence of multiple veils in both LPS-treated samples. **f**, DC

723 differentiation markers (MHC-II and CCR7) of Lfc$^{+/+}$ (blue line) and Lfc$^{-/-}$ (red line) littermate

724 DCs compared to unstained cells (grey peak).

725

726 **Supplementary Figure 4. Lfc$^{-/-}$ DCs exhibit reduced contractile responses. a**, Path choice

727 preference of Lfc$^{+/+}$ and Lfc$^{-/-}$ DCs migrating within a path choice assay. Shown are mean

728 frequencies of Lfc$^{-/-}$ (n = 49 cells of N = 2 experiments) and Lfc$^{+/+}$ (n = 79 cells of N = 3

729 experiments) DCs. **b**, Levels of active RhoA of Lfc$^{+/+}$ and Lfc$^{-/-}$ cells was determined by

730 luminometry showing mean intensities ± S.D. from N = 3 experiments. **** P ≤ 0.0001. **c**,

731 Levels of MLC phosphorylation in Lfc$^{+/+}$ and Lfc$^{-/-}$ DCs assessed by Western Blot analysis. Cells

732 were treated with the indicated compounds (DMSO, CCL21, nocodazole, Y27632 together

733 with nocodazole). **d**, Mean fluorescence intensity of phospho-MLC was normalized to GAPDH

734 signal and shown as fold increase relative to DMSO control ± S.D. Blots are representative of

735 N = 3 experiments. **e**, Centrosome localization in Lfc$^{-/-}$ DCs migrating under agarose assessed

736 by alpha- and gamma-tubulin co-staining (n = 117 cells from N = 2 experiments). **f**, MT

737 nucleation from centrosomal origin as determined by alpha- and gamma-tubulin co-staining.

738 Scale bars, 10μm. **g**, Intensity line scans across the highest gamma-tubulin signal along the

739 left-right axis (dashed line in **f**). The purple line indicates gamma-tubulin signal intensity. The

740 black line indicates alpha-tubulin signal distribution. **h**, Frequency of cell rupturing events of

741 Lfc$^{+/+}$ (n = 73 cells, N = 3 experiments) and Lfc$^{-/-}$ (n = 128 cells, N = 3 experiments) DCs while

742 migrating within single constriction containing microchannels.

743

744   **Supplementary Figure 5. Aberrant spatiotemporal MLC accumulation and moesin**

745   **localization in Lfc$^{-/-}$ DCs. a**, Time-lapse montage of a MLC-GFP expressing DC migrating under

746   agarose towards a soluble CCL19 gradient. A cycle of migration, retraction, and pausing is

747   shown. Scale bar, 10μm. Dotted lines indicate positions further analyzed by Kymograph in **b**.

748   **b**, Leading edge kymograph was derived from grey dotted line in leading edge region of **a**.

749   Trailing edge kymograph was derived from purple dotted line in trailing edge region of **a**. Note

750   the absence of MLC accumulation in leading edge areas and the presence of trailing edge MLC

751   accumulation during migration Scale bar, 5μm. **c**, Time-lapse sequence showing

752   spatiotemporal MLC accumulation of a Lfc$^{+/+}$ DC and **d**, a Lfc$^{-/-}$ DC. Purple arrowheads highlight

753   trailing edge MLC accumulation, orange arrowheads indicate central MLC accumulation. Scale

754   bars, 10μm. **e**, Quantitative morphometry of Moesin in fixed migratory Lfc$^{+/+}$ (red) and Lfc$^{-/-}$

755   (blue) DCs. Lower panel: Quantification of fluorescence intensity in leading versus trailing

756   edge regions of Lfc$^{+/+}$ (red) and Lfc$^{-/-}$ (blue) DCs of n = 55 cells per condition from N = 3

757   experiments. Boxes extend from 25th to 75th percentile. Whiskers span minimum to maximum

758   values. *** P ≤ 0.001, **** P ≤ 0.0001. Scale bars, 10μm. **f**, Protein levels of phospho-ERM

759   in Lfc$^{+/+}$ and Lfc$^{-/-}$ DCs assessed by Western Blot analysis. Right panel: Quantification of pERM

760   levels upon treatment with DMSO, CCL19, nocodazole or Y27632. Mean fluorescence

761   intensity of pERM signal was normalized to total ERM signal and shown as fold increase

762   relative to Lfc$^{+/+}$ DMSO control ± S.D. of N = 3 experiments.

763

764   **Supplementary Figure 6. Unprocessed western blot scans. a**, Raw image of blot probed

765   against GEF-H1. Blue boxed region indicates area shown in Supplementary Fig. 5f. **b**, Raw

766   image of blot probed against phospho-ERM proteins. Blue boxed region indicates area shown

767   in Supplementary Fig. 5f. **c**, Raw image of blot probed against total ERM protein. Blue boxed

768   region indicates area shown in Supplementary Fig. 5f. **d**, Raw image of blot probed against

769   GEF-H1 and phosho-MLC. Blue boxed regions indicate areas shown in Supplementary Fig. 4c.

770   **e**, Raw image of blot probed against GAPDH. Blue boxed region indicates area shown in Fig.

771   Supplementary 4c. **f**, Raw image of blot probed against phosho-MLC. Blue boxed regions

772   indicate areas shown in Supplementary Fig. 2i. **g,** Raw image of blot probed against GAPDH.

773   Blue boxed region indicates area shown in Supplementary Fig. 2i.

774

Supplementary Movie Legends

Supplementary Movie 1. MT dynamics during path finding within a pillar array. An EB3-mCherry expressing reporter cell was acquired while migrating within a complex 3D pillar array towards a soluble CCL19 gradient in 2sec intervals on an inverted spinning disc microscope. Scale bar, 10μm.

Supplementary Movie 2. Polarized MT dynamics in migratory DCs. DC is expressing EMTB-mCherry. Migration during 2D confinement under agarose was acquired in 2sec intervals using a TIRF setup. For representation, the signal was inverted after the acquisition. The upper panel shows the protruding leading edge, in which grey arrowheads indicate elongating MT filaments. The lower panel shows retracting trailing edge of the same cell in which purple arrowheads highlight MT shrinking events. Time in [min:sec]. Scale bar, 5μm.

Supplementary Movie 3. Induced MT depolymerization locally activates the contractile module. TAMRA stained DCs migrating under agarose were recorded every 2sec on an inverted spinning disc microscope and locally photo-activated (red box) every 40sec using a 405nm laser line. Cells were either untreated (upper panel) or treated with PST-1 (lower panel). Time in [min:sec]. Scale bar 10μm.

Supplementary Movie 4. MTs promote cell coherence during migration in complex environments. DCs were either non-treated (control) or treated with the indicated compounds (nocodazole or double treatment using Y27632 together with nocodazole) and recorded while migrating within a path choice assay towards a soluble CCL19 gradient in 60sec intervals. Note that under all conditions cells insert multiple protrusions into different channels when reaching the junction point (black arrowheads). Red arrowheads highlight rupturing events and loss of cellular coherence only observed in drug-treated cells. Time in [min:sec]. Scale bar, 10μm.

Supplementary Movie 5. Perturbation of MT and myosin dynamics impairs DC migration in complex scaffolds. Mature DCs migrating along a soluble CCL19 gradient within a 3D collagen matrix. Shown are separately acquired bright field movies of control- (DMSO), nocodazole-treated and double-treated cells using Y27632 and nocodazole (Y/N) reconstructed in a single

28

807   file. Images were acquired every 60sec for 5h and are represented as single movie in 4min

808   intervals. Time in [min:sec]. Scale bar, 100µm for representative movie of bulk cell movement,

809   scale bar, 10µm for movie showing single cell dynamics.

810

811   **Supplementary Movie 6. Perturbation of MT and myosin dynamics permits DC migration**

812   **within simple linear microenvironments.** Mature DCs migrating along a soluble CCL19

813   gradient within a straight microchannel. Shown are separately acquired bright field movies of

814   non-treated, nocodazole-treated and double-treated cells using Y27632 and nocodazole cells

815   reconstructed in a single file. Images were acquired in 20sec intervals for 5h. Note the

816   frequent directional oscillations of nocodazole only treated cells. Time in [min:sec]. Scale bar,

817   10µm.

818

819   **Supplementary Movie 7. Microtubules mediate retraction of supernumerary protrusions**

820   **via Lfc.** Lfc$^{+/+}$ and Lfc$^{-/-}$ DCs were recorded while migrating within a path choice assay towards

821   a soluble CCL19 gradient in 30sec intervals. Note that both genotypes insert multiple

822   protrusions into different channels when reaching the junction point (black arrowheads). Red

823   arrowheads highlight rupturing events and loss of cellular coherence only observed in Lfc-

824   deficient cells. Time in [min:sec]. Scale bar, 10µm.

825

826   **Supplementary Movie 8. Lfc specifies myosin localization at the trailing edge.** Combined

827   movies of MLC-GFP expressing Lfc$^{+/+}$ DCs (left panel) and Lfc$^{-/-}$ DCs (right panel) migrating

828   under agarose along a soluble CCL19 gradient, acquired in 2sec intervals on an inverted

829   spinning disc microscope. Magenta arrowhead indicates trailing edge MLC accumulation,

830   which is absent in Lfc$^{-/-}$ cells. Orange arrowhead highlights central MLC accumulation.

831   Fluorescence signal was inverted for better visualization. Time in [min:sec]. Scale bar 10µm.

832

833   **Supplementary Movie 9. Lfc promotes DC migration within complex environments.** Mature

834   DCs generated from Lfc$^{+/+}$ and Lfc$^{-/-}$ mice were embedded in a 3D collagen matrix. Migration

835   along a soluble CCL19 gradient was acquired for 5h in 1min intervals. Images for each

836   condition were subsequently reconstructed as a single file in 4min intervals. Time in [min:sec].

837

838   **Supplementary movie 10. Lfc regulates MT-mediated adhesion resolution.** Nocodazole-

839   treated Lfc$^{+/+}$ and Lfc$^{-/-}$ DCs were acquired while migrating under agarose towards a soluble

840   CCL19 gradient in 20 second intervals on an inverted cell culture microscope. Left panels show

841   nocodazole-treated cells during adhesive migration. Note the loss of directionality in Lfc$^{+/+}$

842   DCs and the pronounced elongation of Lfc$^{-/-}$ DCs. Right panels show nocodazole effects during

843   adhesion-independent migration on PEG coated coverslips. Note the persistent loss of

844   directionality in Lfc$^{+/+}$ DCs but the restored cell lengths of of Lfc$^{-/-}$ DCs. Time in [min:sec]. Scale

845   bar 100µm.

Microtubules control cellular shape and coherence in amoeboid migrating cells

Figure 1 - The microtubule organizing center acts as pathfinder by coordinating protrusion dynamics
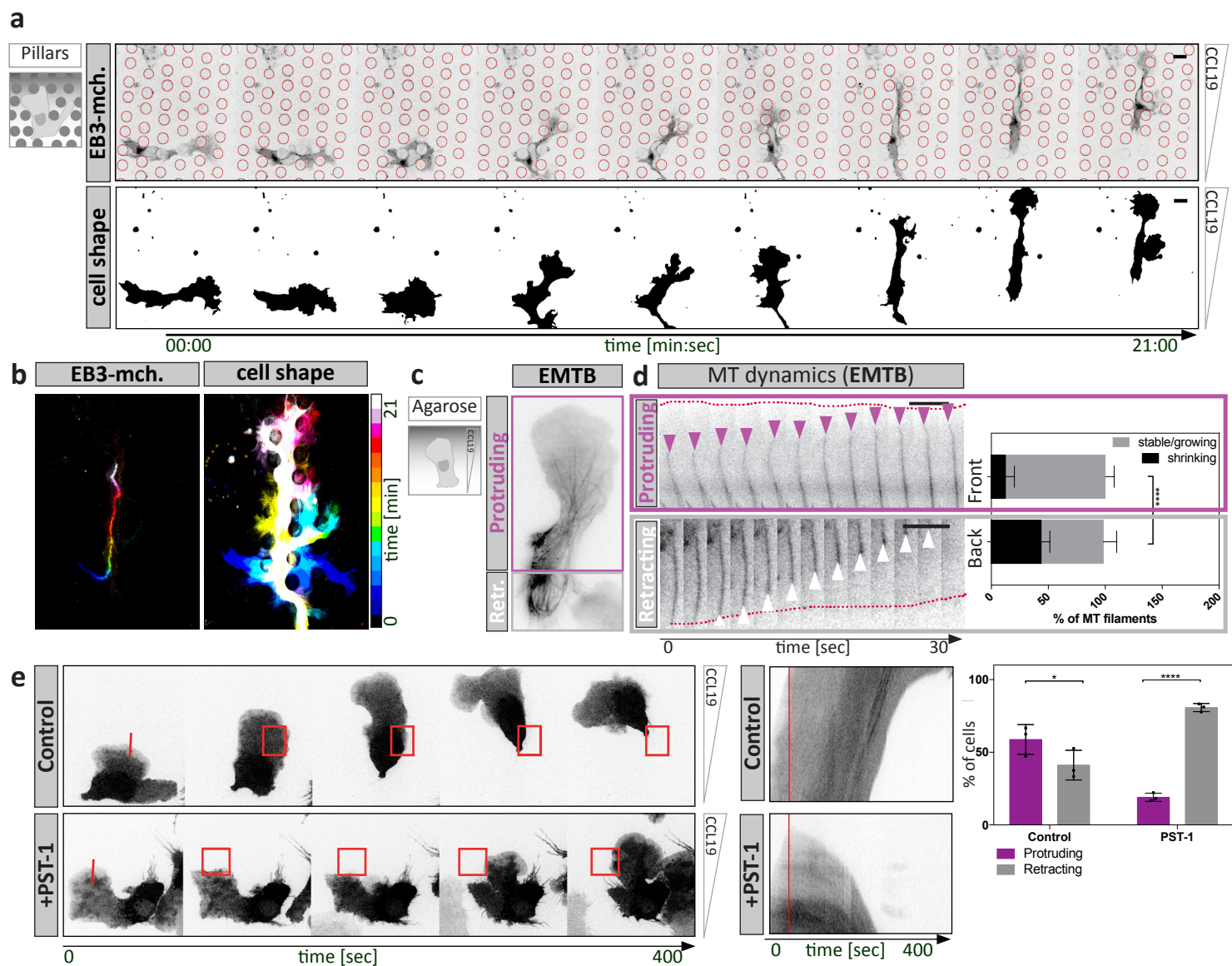
Microtubules control cellular shape and coherence in amoeboid migrating cells

Figure 2 - Microtubules coordinate protrusion dynamics via the contractile module
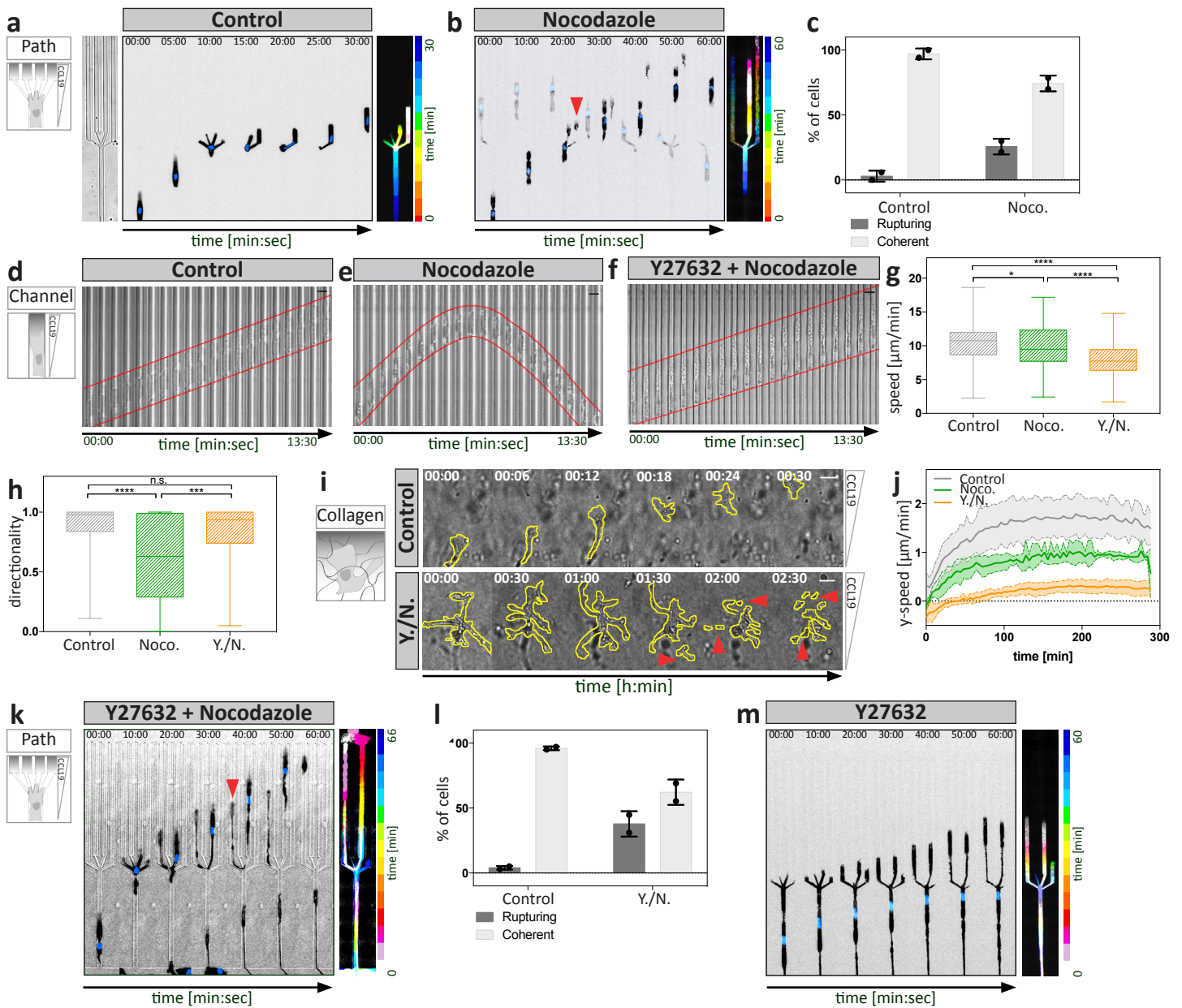
Microtubules control cellular shape and coherence in amoeboid migrating cells

Figure 3 - Microtubules mediate retraction of supernumerary protrusions via Lfc
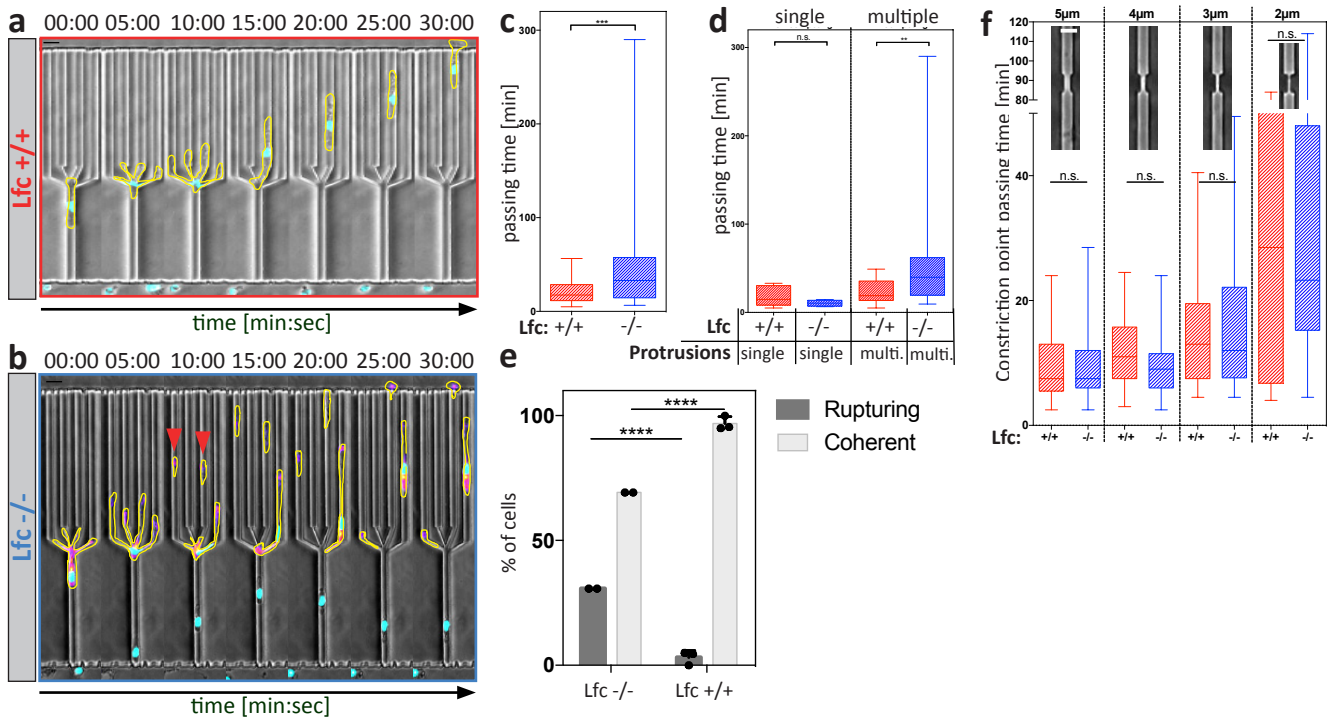
Microtubules control cellular shape and coherence in amoeboid migrating cells

Figure 4 - Lfc-dependent myosin accumulation controls cellular locomotion
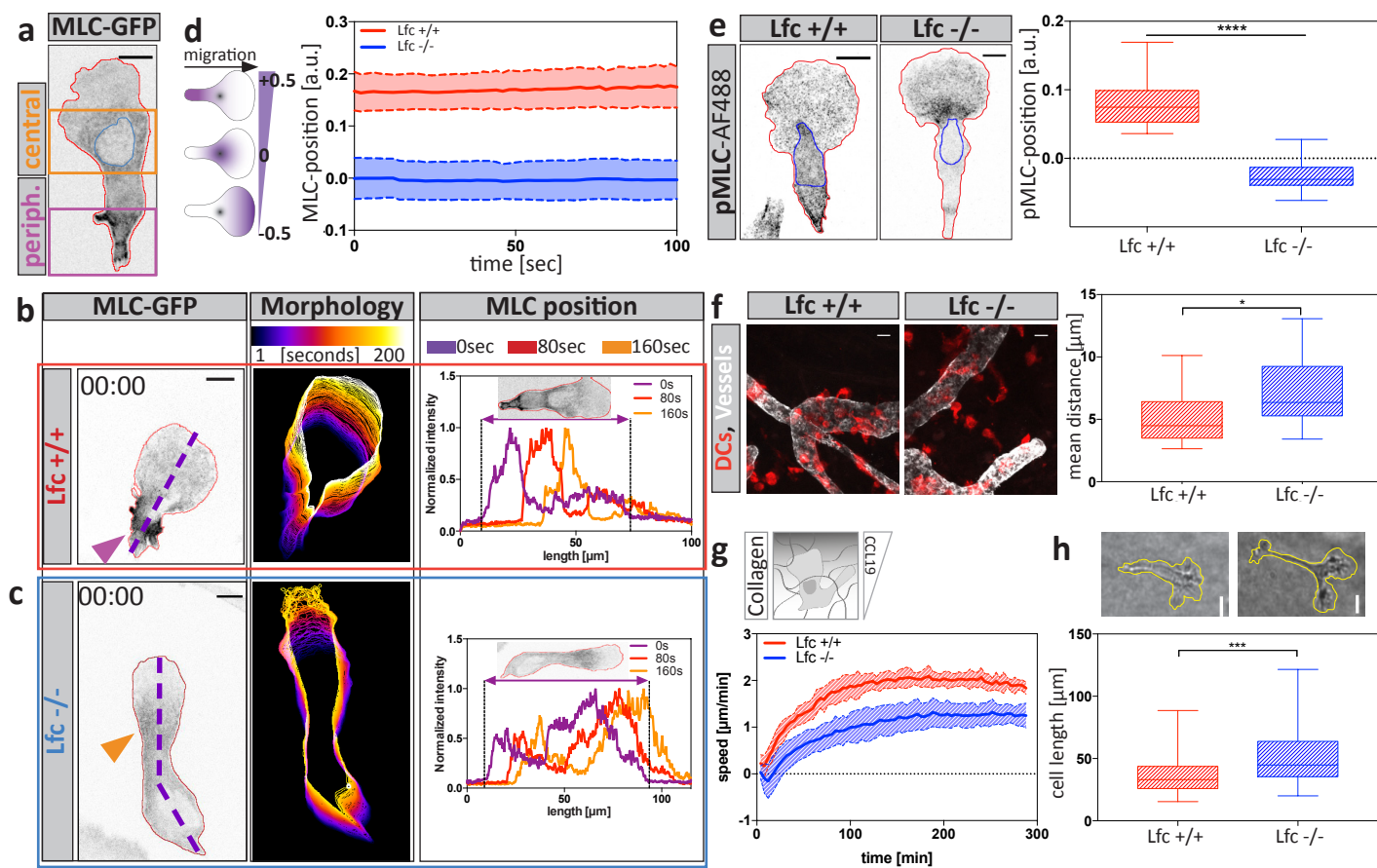
Microtubules control cellular shape and coherence in amoeboid migrating cells

Figure 5 - Lfc regulates microtubule-mediated adhesion resolution
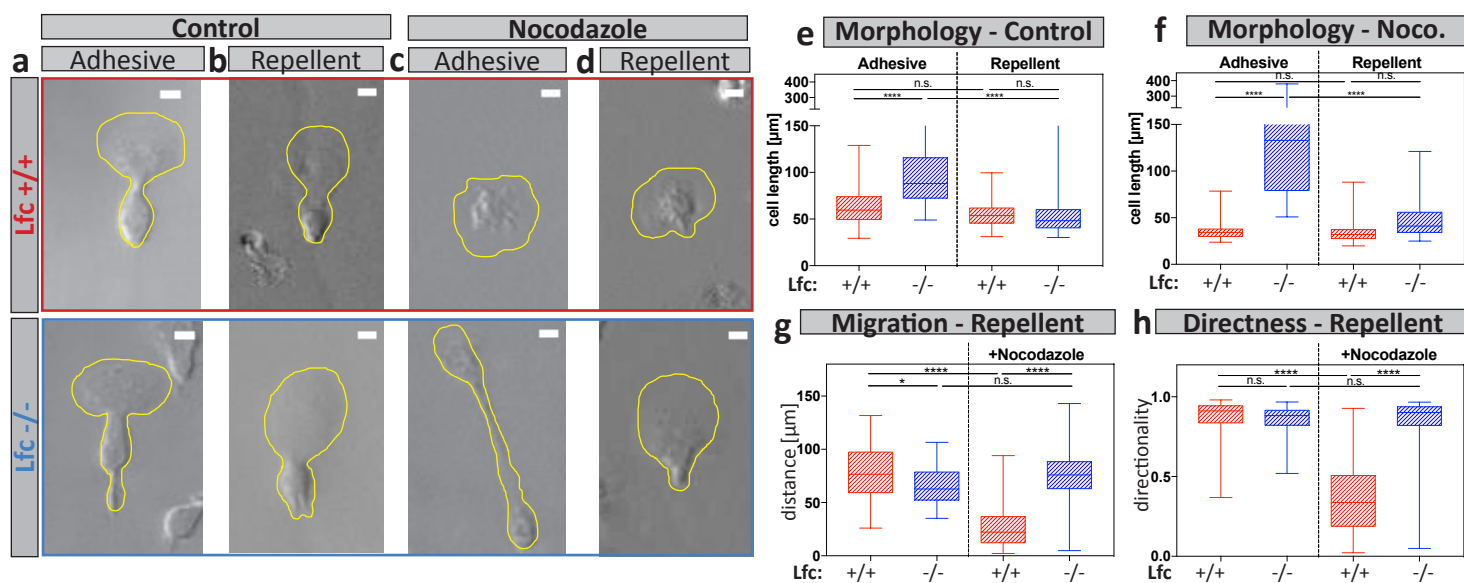
Microtubules control cellular shape and coherence in amoeboid migrating cells

Supplementary Figure 1 - DC migration within diverse matrices to study the role of the MT cytoskeleton during amoeboid migration.
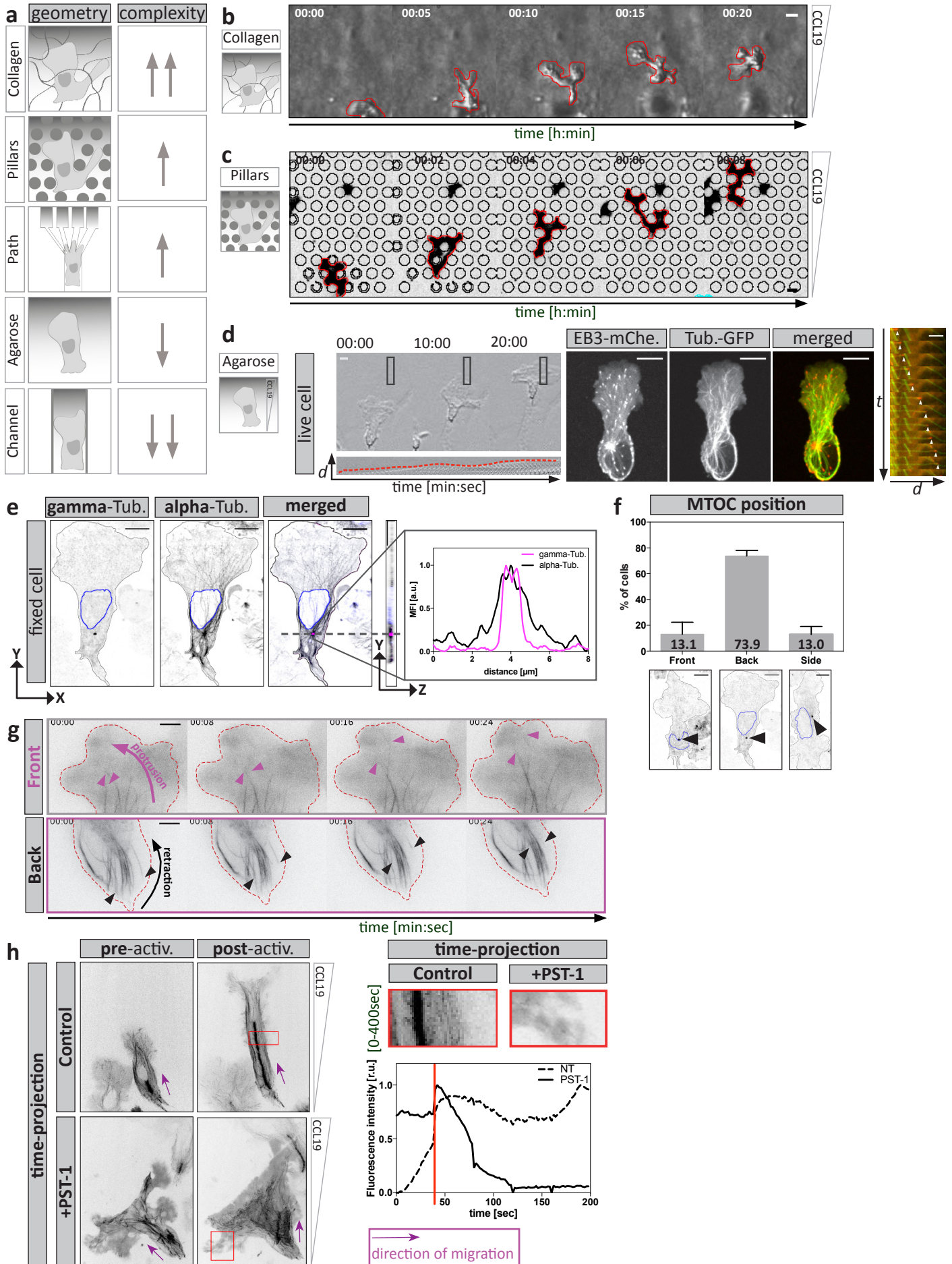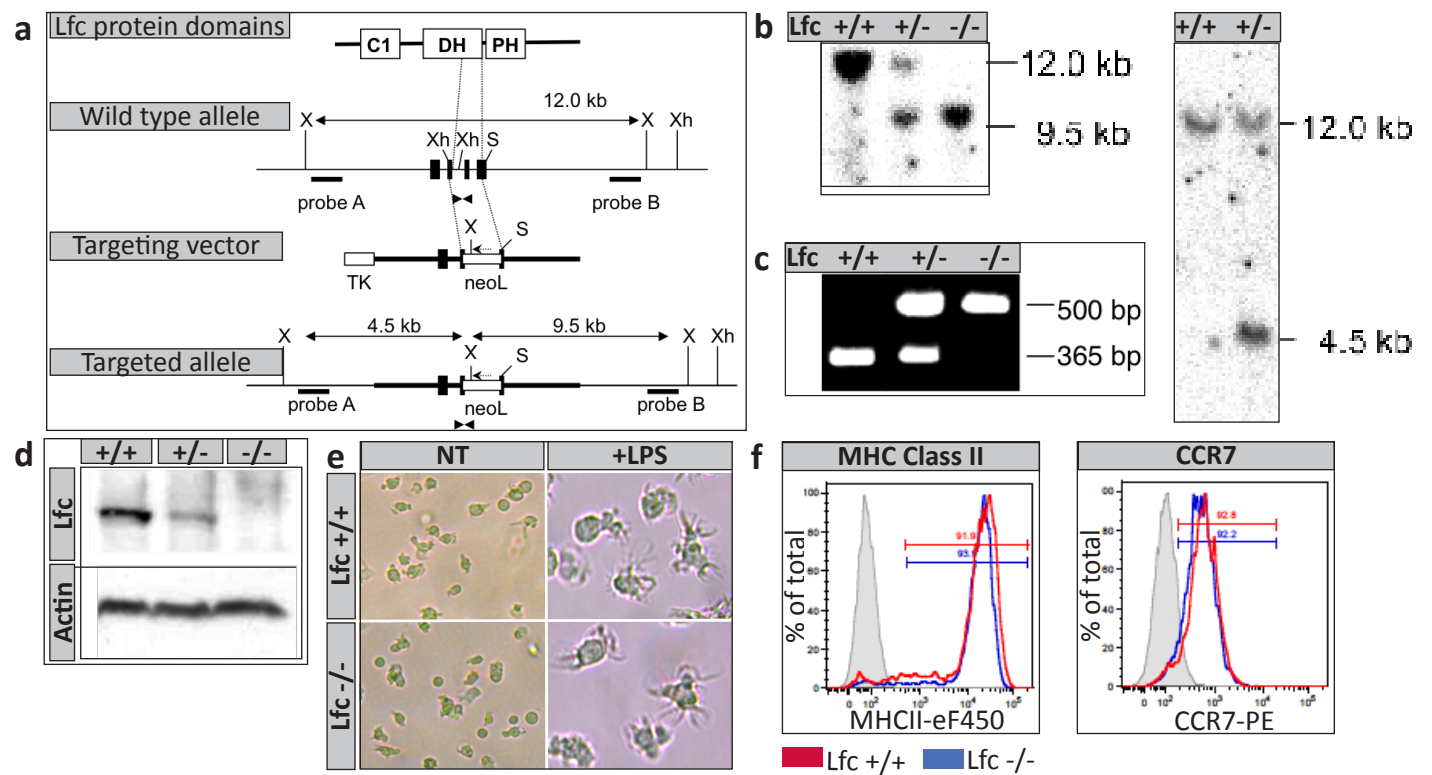
Microtubules control cellular shape and coherence in amoeboid migrating cells

Supplementary Figure 2 - Perturbation of the MT cytoskeleton affects DC migration on multiple levels.
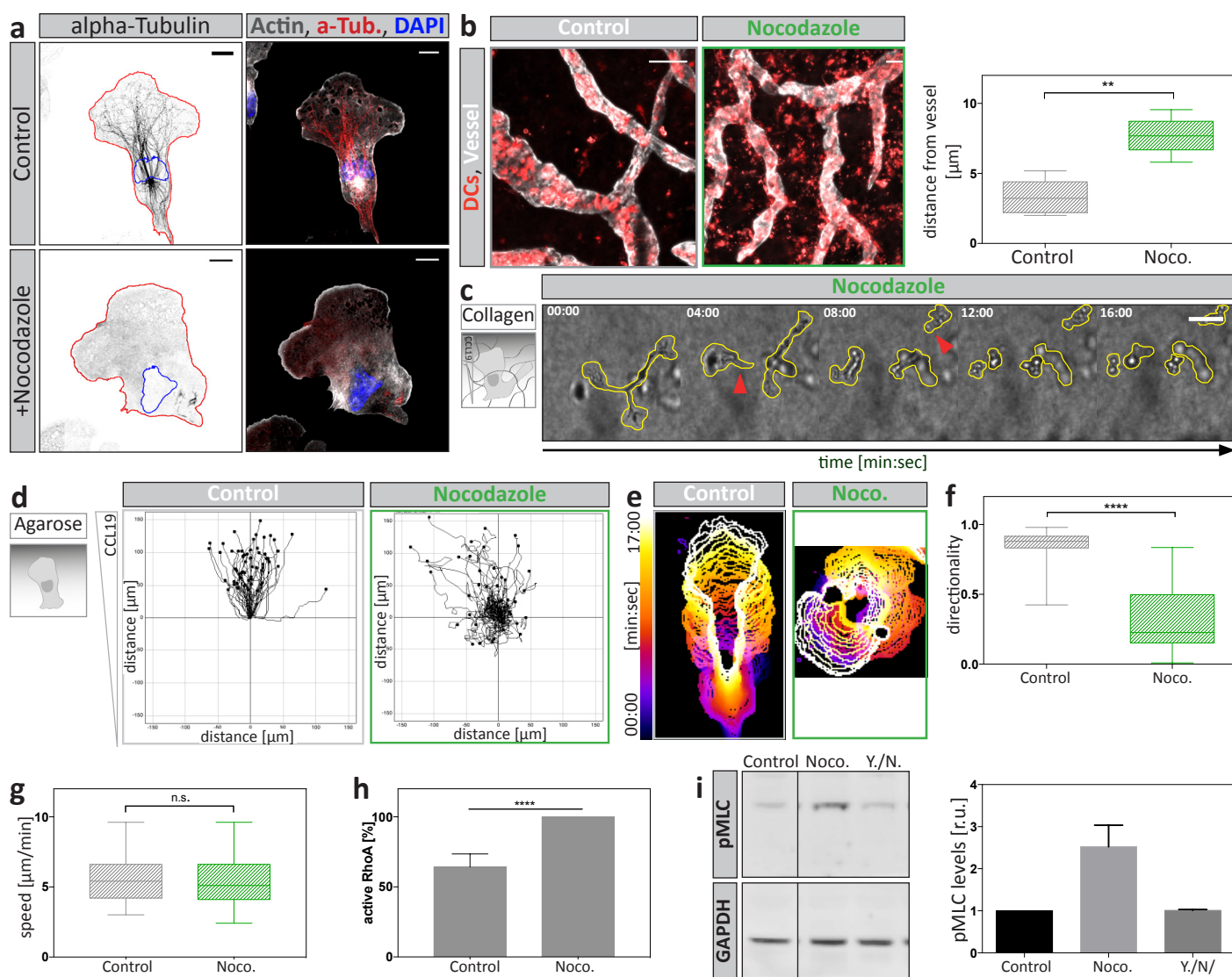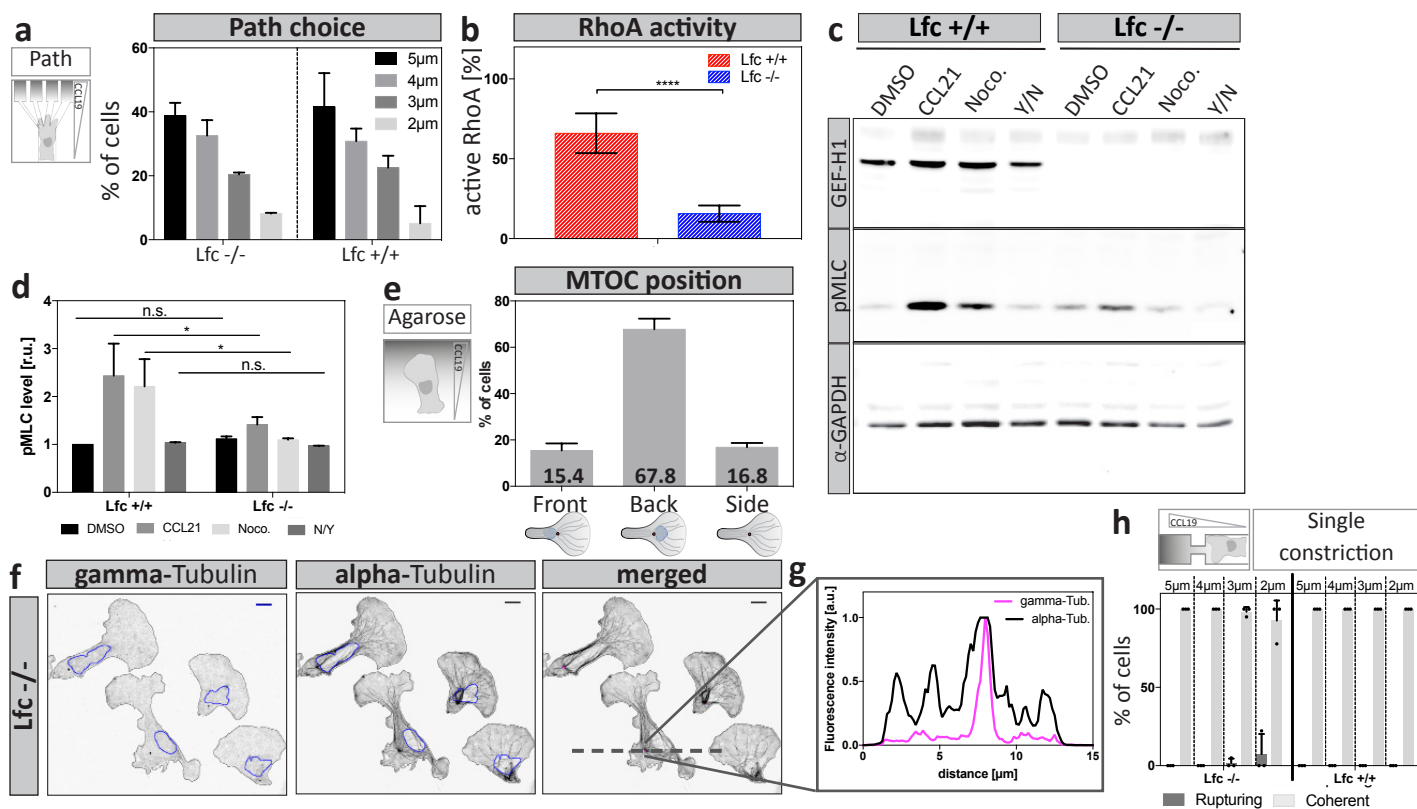
Microtubules control cellular shape and coherence in amoeboid migrating cells

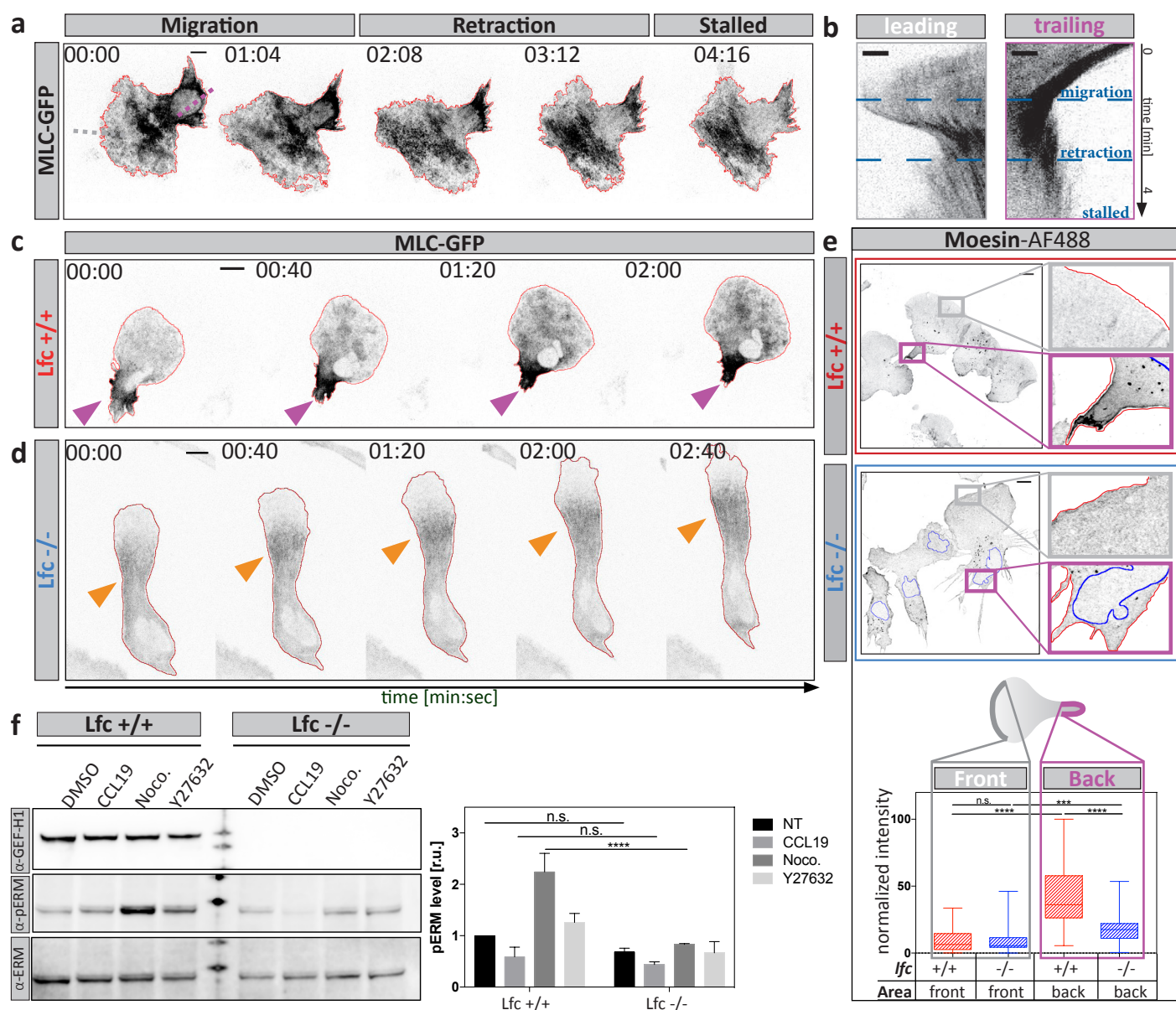**Supplementary Figure 3** - Generation of a Lfc-deficient mouse line.

Microtubules control cellular shape and coherence in amoeboid migrating cells

Supplementary Figure 4 - Lfc-deficent DCs exhibit reduced contractile responses.

Microtubules control cellular shape and coherence in amoeboid migrating cells

Supplementary Figure 5 - Aberrant spatiotemporal MLC accumulation and moesin localization in Lfc-deficient DCs.

Microtubules control cellular shape and coherence in amoeboid migrating cells

Supplementary Figure 6 - Unprocessed western blot scans.